Journal of Structural Geology 190 (2025) 105293

Contents lists available at ScienceDirect

Journal of Structural Geology

journal homepage: www.elsevier.com/locate/jsg

Evidence for an aseismic gap between the Mw6.8 Pütürge (Elazığ) and 7.8 Pazarcık (Kahramanmaraş) earthquakes in the east Anatolian fault system, southeast Türkiye

Elif Akgün [a,*], Savaş Topal [b], Mustafa Softa [c,f], Murat Nas [d], Serkan Gürgöze [e], Hasan Sözbilir [c], Ercan Aksoy [a], Joel Q.G. Spencer [f], Mehmet Yüksel [g]

[a] Faculty of Engineering, Geology Engineering, Fırat University, 23110, Elazığ, Türkiye
[b] Faculty of Engineering, Geology Engineering, Pamukkale University, 20160, Denizli, Türkiye
[c] Faculty of Engineering, Geology Engineering, Dokuz Eylül University, 35390, İzmir, Türkiye
[d] Department of Civil Engineering, Karadeniz Technical University, 61080, Trabzon, Türkiye
[e] Department of Geography, Ondokuz Mayıs University, 55139, Samsun, Türkiye
[f] Department of Geology, Kansas State University, Manhattan, KS, 66506, USA
[g] Faculty of Science and Letters, Physics, Çukurova University, 01250, Adana, Türkiye

ARTICLE INFO

Keywords:
Pütürge segment
East Anatolian fault system
Morphometric index
Kinematic analysis
Kahramanmaraş earthquakes

ABSTRACT

This study examines the unruptured portion of the Pütürge segment, the least-studied section of the East Anatolian Fault System (EAFS) in southeast Türkiye, focusing on the Şiro Valley to comprehensively understand the observed distribution in deformation. Despite the February 6, 2023 doublet earthquakes, the Pütürge segment near the Şiro Valley remained relatively stable, though significant stress accumulation was detected at both ends. Fieldwork and subsequent morphometric and structural analyses confirmed notable tectonic activity in the area. Geomorphic indices were applied to assess tectonic activity, yielding an average index of relative tectonic activity (Iat) for all drainage basins, highlighting varying tectonic intensity levels across the Şiro Valley. Mountain front sinuosity (Smf) analysis indicated different uplift rates and tectonic forces along distinct fault segments. Additionally, Hypsometric Integral-Hypsometric Curve (HI-HC) index analysis pointed to rapid uplift processes, particularly in the eastern part of the fault-controlled basin, signaling active tectonic uplift and geomorphic rejuvenation. Normalized steepness index (ksn) and Chi (χ) values highlighted variations in erosion rate, providing insight into regional uplift patterns and knickpoint distributions. These findings align with the dominant transtensional tectonic regime in the area, as inferred from slip data inversions along the Şiro Valley. The region's fault geometry, oblique movement, and block rotations firmly support this interpretation. Comparisons of slip rates and ground deformation models revealed notable variations in fault behavior, suggesting ongoing energy accumulation, possibly linked to aseismic creep. The complex fault system behavior was underscored by the 2020 Sivrice earthquake and the 2023 doublet, which highlights the critical role of the Pütürge segment in the dynamic evolution of the EAFS.

1. Introduction

Earth's dynamics continually sculpt its features via a powerful interplay of tectonic mechanisms and geomorphological processes (Dasgupta et al., 2023). This continual interplay, which innately shapes landscapes and influences geological processes, remains a crucial study area for understanding the complex behavior on Earth's surface and subsurface. Of the tools that help us delve into these complex relationships, tectonic geomorphology has come to the fore and mainly investigates the delicate balance and vigorous interactions between the tectonic and geomorphic processes (Mayer, 1986; Whipple and Tucker, 1999; Willett et al., 2006; Scotti et al., 2014). Geomorphic indices and quantitative geomorphological analysis, coupled with strong ground-motion seismology, can be employed to identify and assess tectonic zones, providing insights into relative tectonic activity rates and active tectonic processes (Keller, 1986; Keller and Pinter, 1996). In this

* Corresponding author.
E-mail address: efiratligil@firat.edu.tr (E. Akgün).

https://doi.org/10.1016/j.jsg.2024.105293
Received 31 August 2024; Received in revised form 7 November 2024; Accepted 14 November 2024
Available online 16 November 2024

study, we used these quantitative and qualitative tools to portray the nature of Türkiye's unruptured, hence least studied, fault segment.

One particular region distinctly stands out in the mosaic of Türkiye's geological diversity due to its exceptional geographical and geological characteristics. East Anatolia, characterized by its rheological heterogeneity, has a complex structural geometry influenced by compressional and strike-slip tectonic regimes (Muehlberger and Gordon, 1987; Lyberis et al., 1992). The East Anatolian Fault System (EAFS) epitomizes the dynamic interactions between the converging Arabian plate and the Anatolian block, facilitating the westward motion of the latter—a process termed oblique convergence and indentation tectonics (Lyberis et al., 1992).

Such transcurrent strike-slip fault zones generate significant seismic activity, as they accommodate substantial deformation and indentation tectonics. Despite being seismically less active than the North Anatolian Fault Zone (NAFZ) during the 20th century (Ambraseys, 1989), the EAFS demonstrated potential for significant seismic events, such as the Mw 6.8 (AFAD, 2023) Sivrice (Elazığ) earthquake in 2020, which occurred in the northeastern part of the Pütürge segment (Fig. 1). In the aftermath of the 2020 quake, Coulomb analyses coupled with interferometric synthetic aperture radar (InSAR) images revealed the occurrence of stress transfer to both the northeastern and southwestern strand tips of the EAFS (Tatar et al., 2020; Kürçer et al., 2020).

Among the several key segments, the Pazarcık segment is recognized for its significant seismic gap, determined from paleoseismological data (Yönlü et al., 2012). Recent seismic activity culminated with the Pazarcık (Kahramanmaraş) earthquake on February 6, 2023, which registered magnitudes of Mw 7.8 (USGS, 2023) and Mw 7.7 (AFAD, 2023). This event ruptured the Pazarcık segment and, although not yet clear, is believed to have triggered another significant quake in the Ekinözü (Elbistan/Kahramanmaraş) zone of the Çardak and Doğanşehir segment (Softa et al., 2024). Located on the northern strand of the EAFS, this subsequent earthquake registered magnitudes of Mw 7.5 (USGS, 2023) and Mw 7.6 (AFAD, 2023), occurring on the same day, approximately 9 h later. As a result of the Mw 7.7 Pazarcık earthquake, which occurred in the primary strand of the EAFS, the Amanos, Narlı, Pazarcık, and Erkenek segments experienced massive rupturing, resulting in a 270-km-long surface rupture (Karabacak et al., 2023; Aksoy et al., 2023; Gürboğa et al., 2024). The surface projection of the rupture driven by the Pazarcık earthquake is visually traceable in the Çelikhan (Adıyaman) district at the northeastern end of the Erkenek segment (Karabacak et al., 2023; Aksoy et al., 2023). Notably, InSAR data from the earlier Sivrice earthquake in 2020, show that approximately 40 km of the Pütürge segment ruptured up to the Ormaniçi (Malatya) settlement, although no surface rupture was observed in field studies (Tatar et al., 2020). While InSAR data (Tatar et al., 2020; Karslıoğlu et al., 2021) suggest significant vertical displacement from fault rupture, the absence of corresponding net slip or clear ground movement at the precise field locations presents a compelling enigma.

Upon the devastating doublet earthquake on February 6, 2023, the motivation and impetus behind this study became undeniable and nondeferrable. Following extensive fieldwork involving an international team of scientists from various disciplines, this study aims to integrate morphometric and structural analyses with current and model-based averaged long-term deformations. Its primary objective is to elucidate the distribution of deformation along the as-yet unruptured segments of the Pütürge Segment in the Şiro Valley (pronounced as Shiro), making it an optimal location for studying Holocene active faulting and conducting the most comprehensive study of the area to date. Two critical factors—the lack of significant surface rupture during the 2020 Sivrice earthquake and the abrupt termination of deformed fault traces in the Şiro Valley—underscore the complexities of the Eastern Anatolian Fault System and highlight the need for further investigation into the unruptured Pütürge segment. Additionally, it seeks to address lingering questions, minimize uncertainties, and potentially uncover new ones.

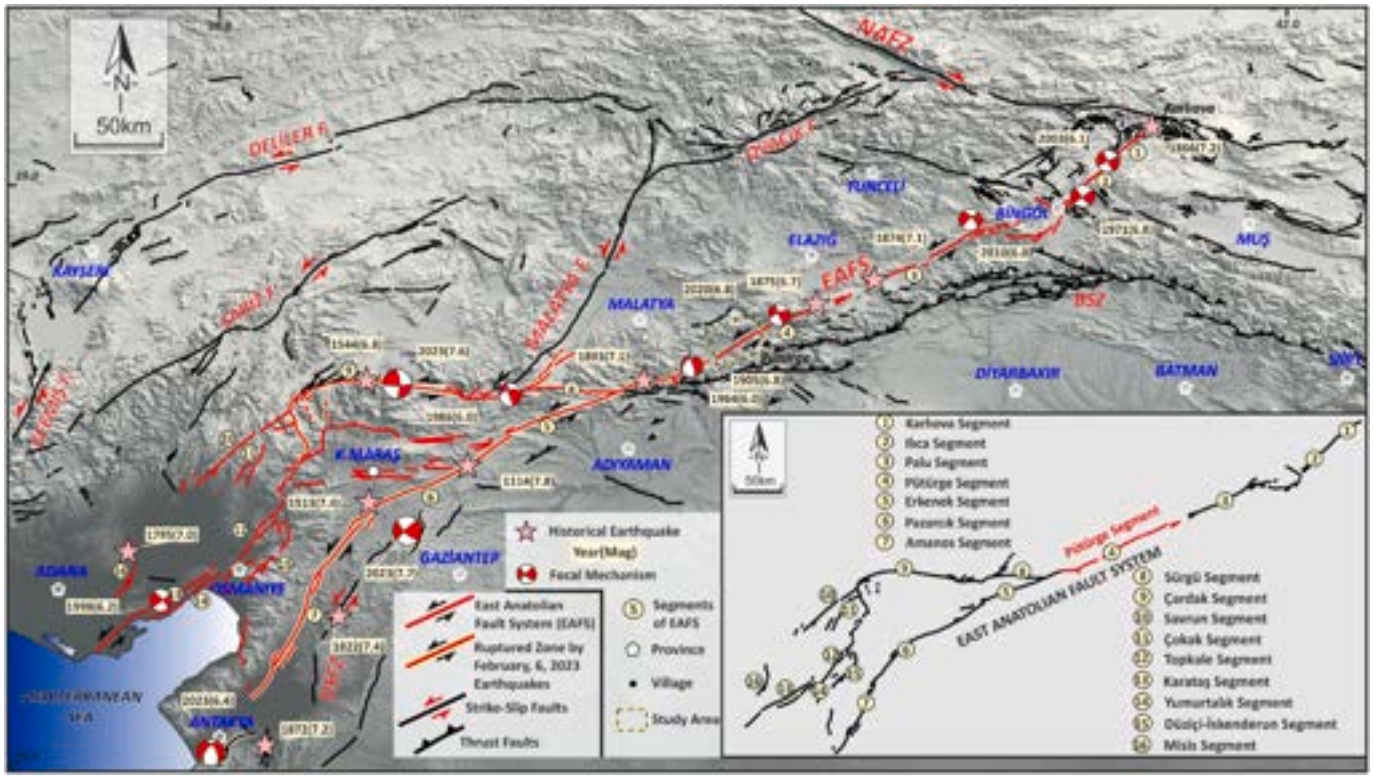

Fig. 1. Tectonic framework (Duman and Emre, 2013) of eastern Türkiye with historical (Ambraseys, 1989; Ambraseys and Finkel, 1995; Ambraseys and Jackson, 1998; Tan et al., 2008) and instrumental (AFAD, 2023) earthquakes along the East Anatolian Fault System (EAFS). The inset shows a detailed segmentation of branches along the EAFS. NAFZ-North Anatolian Fault Zone, DSFZ-Dead Sea Fault Zone.

2. Geological and seismotectonic setting

East Anatolia underwent deformation as a result of the subduction of the northern and southern branches of the Neotethys Ocean during distinct convergence stages from the Cretaceous period to the present day (McKenzie, 1972, 1978; Şengör and Yılmaz, 1981; Şengör et al., 1985). During these deformational phases, nappe packages consisting of various units, including metamorphic, ophiolitic, somewhat entwined, and complex formations, were emplaced and accreted onto the Arabian plate (Yılmaz, 1993). At the end of the Middle Miocene, marking the onset of the neotectonic period in Türkiye, the closure of the southern branch of the Neotethys along the Bitlis Suture Zone (BSZ) in East Anatolia initiated continent-continent collision, thereby massively shaping the geological evolution of the region (Ketin, 1948; McKenzie, 1970, 1972, 1978; Şengör, 1980; Şengör and Yılmaz, 1981). This collision resulted in the deformation of East Anatolia into compressive folds and thrusts along the BSZ, a process that continued until the end of the Pliocene. The ongoing collision and convergence led to uplift and exhumation of the East Anatolian high plateau, characterized by east–west-trending fold and thrust structures, which persisted until the end of the Pliocene. By the late Pliocene, the NAFZ and EAFS were the primary agents of intracontinental deformation in East Anatolia (Şengör, 1980; Şengör et al., 1985). The EAFS, delineating the plate boundary between the Arabian plate and Anatolian block, is thus an intracontinental strike-slip fault zone characterized by sinistral motion.

The EAFS intersects with the NAFZ at the Karlıova triple junction and consists of numerous left-lateral strike-slip faults trending approximately northeast–southwest. There is widespread consensus on the spatial initiation of the EAFS. However, some studies (Arpat and Şaroğlu, 1975; Şengör et al., 1985; Kiratzi, 1993; Şaroğlu et al., 1992) have proposed its connection with the Dead Sea Fault Zone (DSFZ), while others (Lovelock, 1984; Muehlberger and Gordon, 1987; Perinçek and Çemen, 1990; Yürür and Chorowicz, 1998) contend that it intersects at the Türkoğlu (Kahramanmaraş) triple junction. Most researchers assert that the EAFS extends into the Mediterranean region (McKenzie, 1970, 1972; Barka and Kadinsky-Cade, 1988; Taymaz et al., 1991; Westaway, 1994; Westaway and Arger, 1996; Arger et al., 2000).

The EAFS is typically characterized by its changing orientation, which has led to the defining of a series of segments by numerous researchers who have identified distinct sections based on bending and stepover features (Arpat and Şaroğlu, 1975; Barka and Kadinsky-Cade, 1988; Şaroğlu et al., 1992; Herece, 2008; Duman and Emre, 2013). In terms of movement, while some researchers reported a total offset of 15 km (Seymen and Aydın, 1972) along the EAFS, others (Arpat and Şaroğlu, 1972) suggested that the fault slip within the Göynük valley ranged between 22 and 27 km. In addition, stream offsets indicating Quaternary activity are observed from 10 m to 3 km along the EAFS.

The initiation of the EAFS is widely accepted as late Pliocene based on the offsets observed along the fault (Arpat and Şaroğlu, 1972; Şengör and Yılmaz, 1981; Şengör et al., 1985; Dewey et al., 1986; Hempton, 1987; Perinçek and Çemen, 1990; Lyberis et al., 1992; Westaway and Arger, 2001; Aksoy et al., 2007). However, some studies (Herece and Akay, 1992; Herece, 2008) have proposed the late Pliocene-Pleistocene boundary for the beginning of the EAFS, particularly considering that E-W-oriented folds developed in the Pliocene basins in the northeastern part of the fault zone.

The Pütürge segment, an integral part of the EAFS, trends approximately N55°-65°E and extends from the Lake Hazar releasing bend to the Yarpuzlu restraining bend. This segment is distinguished by its narrow deformation zone along the Euphrates River, where deep valleys have formed due to the predominant strike-slip fault morphology (Çetin and Güneyli, 2002). Notably, the Pütürge segment is characterized by a broader deformation zone within the Şiro Valley, where the strike-slip tectonic regime consists of strike-slip to dip-slip faults, indicating complex interactions between different tectonic stresses (Çetin and Güneyli, 2002; Akgün and İnceöz, 2021). In the historical period, the Pütürge segment has been seismically active, with significant earthquakes recorded near both ends of the segment: a magnitude 6.7 earthquake in 1875 near the northeastern end and a magnitude 6.8 earthquake in 1905 near the southwestern end (Ambraseys, 1989; Ambraseys and Jackson, 1998; Duman and Emre, 2013; Duman et al., 2018).

3. Methodology

3.1. Inversion for stress

Stress inversion analysis, a crucial method in structural geology, involves restoring paleostress patterns using fault-slip datasets (Angelier, 1994; Vanik et al., 2018). Along the fault segments, slip data serve as the cornerstone dataset for revealing fault geometry and deformation history and interpreting the principal characteristics of the regional stress tensor responsible for deformation across a wide area (Carey-Gailhardis and Mercier, 1987).

Two primary methods are employed in stress inversion analysis: graphical methods based on fault theory from Anderson (1951) and numerical methods relying on the Wallace-Bott hypothesis (Wallace, 1958; Bott, 1959). Through these numerical methods, the stress axes ($\sigma1 > \sigma2 > \sigma3$) and stress ratio parameters (R: $(\sigma2 - \sigma3)/(\sigma1 - \sigma3)$, where $0 < R < 1$) governing deformation are calculated (Angelier, 1990). Additionally, the stress ratio parameter, ranging between 0 ($\sigma2 = \sigma3$) and 1 ($\sigma1 = \sigma2$), determines the shape of the deformation ellipsoid (Angelier, 1994).

In this study, fault parameters, such as the direction of the fault plane, dip angle, dip direction, and rake, were determined and measured using a compass along the fault zone. Kinematic indicators such as slickenlines, calcite fibers, fault grooves, and chatter marks played a pivotal role in determining the direction of movement of the fault.

The measured kinematic data were organized into subgroups, each containing at least three measurements. Stress axes and ratios were computed using the rotational optimization method, using WinTensor 5.9.1 software developed by Delvaux and Sperner (2003). This method, based on the principles and procedures of Angelier (1994), employs the misfit angle (α) to gauge the accuracy of the evaluated data. The misfit angle represents the angle between the orientation of the measured fault set and the maximum shear stress resolved on the fault plane. In that sense, the misfit angle is an indicator of the accuracy of the evaluated data. Optimization of the misfit angle aims to minimize the normal stress and maximize the shear stress acting on the fault plane (Delvaux and Sperner, 2003).

The stress regime index (R′) is determined based on the stress ratio (R), which ranges from 0 to 3. In normal fault formations, the stress regime index equals the stress ratio ($R' = R$), with values between 0 and 1. For strike-slip faults, the stress regime index ($R' = 2 - R$) is derived by subtracting the stress ratio value from 2, resulting in values ranging from 1 to 2. In compressional regimes, the stress regime index is calculated by adding 2 to the stress ratio ($R' = 2 + R$) (Delvaux et al., 1997).

The relationship between morphometric uplift rates and kinematic analysis offers a comprehensive understanding of how tectonic forces shape the landscape. Uplift rates quantify vertical movements, while kinematic analysis elucidates the underlying mechanisms driving these movements, such as fault slip and block rotation. In addition, these approaches provide valuable insights into the interaction between tectonic processes and surface deformation (Burbank and Anderson, 2011; Keller and Pinter, 2002).

3.2. Morphometric indices

We carried out a comprehensive analysis to determine the spatial distribution of the quantitative relative tectonic activity index (Iat), using the method proposed by El Hamdouni et al. (2008). The methodological approach was a combination of various morphometric techniques, including the mountain front sinuosity (Smf) and the valley floor

width-to-height ratio (Vf) from Bull and McFadden (1977), the hypsometric integral (HI) and hypsometric curve (HC) as delineated by Keller and Pinter (2002), the asymmetry factor (AF) following the framework of Hare and Gardner (1985), the drainage basin shape (*Bs*) methodology outlined by Cannon (1976), the normalized steepness index (*ksn*), based on the Stream power incision model (SPIM), pioneered by Hack (1957), and the Gilbert metrics and Chi (χ) analyses (see Table 1). These analyses were conducted on drainage basins dominantly influenced by the Pütürge segment, utilizing datasets derived from SRTM maps with a resolution of 4.5 m and 1:25,000 digitized topographic maps. We used ArcGIS software (version 10.2 Pro) and QGIS (version 3.34 LTR) to conduct a comprehensive analysis of these indices, supplemented by MATLAB® R2023b software and using a package called TopoToolbox version 2 (Schwanghart and Kuhn, 2010; Schwanghart and Scherler, 2014), along with river profile analysis codes (Gallen and Wegmann, 2017). In this analsysis the integration of rock quality and strength parameters with morphometric indices is essential. To achieve this, simplified geological maps were digitally prepared at a scale of 1:100,000, sourced initially from the Geological Maps of Türkiye website (https://www.mta.gov.tr/en/maps). These maps facilitated the characterization of rock strength according to the Selby (1980) scales, which encompass a spectrum ranging from high to very low strength categories. Our morphometric data were compared to paleostress data and previously published paleoseismological records. This integration aimed to discern the distribution pattern of the relative tectonic activity index (*Iat*) in association with the active segmentation of the EAFS.

Examining the variable tectonic forces and uplift rates along different segments in the study area is particularly important for understanding the influence of large structural elements such as the EAFS in the region. The variation in tectonic forces along different regional segments can affect local erosion rates and tectonic uplift processes. The Ksn and χ analyses allow a better understanding of these variations and provide essential data for assessing potential hazards, especially in rural areas. In addition to that, uplift rates are commonly estimated using Smf and Vf values. Fault activity and uplift rates can be inferred by analyzing Smf values from mountain fronts near the Pütürge segment and Vf values from its drainage areas. These analyses, especially the Smf and Vf results, help estimate long-term slip rates and understand relative uplift rates through regression, as suggested by Rockwell et al. (1984). Smf, an indicator of both erosion and tectonic activity, reveals varying mountain front patterns across elevation gradients (Rockwell et al., 1984; Koukouvelas et al., 2018), often resulting in broader, sinuous curvatures (Bull and McFadden, 1977).

(1) Mountain front sinuosity index (***Smf***)

The mountain front sinuosity (*Smf*) is a pivotal tool for delineating regions of heightened tectonic activity. This index considers the equilibrium between erosional processes generating irregular or sinuous mountain fronts and tectonic forces creating linear mountain fronts, as represented by equation (1) (Bull and McFadden, 1977):

$$Smf = \frac{Lmf}{Ls} \tag{1}$$

where *Smf* is the mountain front sinuosity, *Lmf* denotes the length of the mountain front, and *Ls* is the length of the straight line connecting the endpoints of the mountain front.

In regions characterized by heightened tectonic activity, the *Smf* values typically fall below 1.4. However, even mountain fronts experiencing relatively subdued tectonic activity exhibit discernible indications of active tectonics, with *Smf* values ranging from 1.4 to 3.0. Conversely, *Smf* values exceeding 3.0 are indicative of inactive fronts (Bull and McFadden, 1977).

(2) Valley floor width–valley height ratio (***Vf***)

The valley floor width-to-height ratio (*Vf*), as represented by equation (2), is a principal geomorphic index used to distinguish between V-shaped and U-shaped valleys and serves as a proxy for active tectonics (Bull and McFadden, 1977).

$$Vf = \frac{2Vfw}{[(Eld - Esc) + (Erd - Esc)]} \tag{2}$$

where *Vf* denotes the valley floor width-to-height ratio, *Vfw* is the valley floor width, *Eld* is the elevation of the left divide, *Esc* is the elevation of the stream channel, and *Erd* is the elevation of the right divide.

A diminished *Vf* signifies an elevated pace of erosion and uplift, leading to the formation of deep V-shaped valleys, wherein tectonic forces predominate over erosional mechanisms. Conversely, an augmented *Vf* value correlates with the presence of a U-shaped valley or a valley exhibiting a flat-bottomed morphology, primarily shaped by bed-level erosional processes.

(3) Asymmetry factor (***AF***)

The asymmetry factor (*AF*), as represented by equation (3) (Hare and Gardner, 1985), holds significance as a parameter in basin drainage analysis to discern the manifestation of tectonic slopes within the basin. The slope development within the basin arises from tectonic perturbations, prompting the primary river channel to deviate from the central axis of the basin toward the direction of slope propagation.

$$AF = 100 \times \frac{Ar}{At} \tag{3}$$

where *AF* is the asymmetry factor, *Ar* denotes the area of the basin to the right of the basin axis, and *At* is the total area of the basin.

An asymmetry factor (*AF*) surpassing or falling short of 50 signifies the influence of either tectonic activity or lithologic control, whereas a value approaching 50 denotes a negligible or minimal slope within the basin.

(4) Hypsometric integral and curve (*HI* and ***HC***)

The hypsometric integral (*HI*), as represented by equation (4) (Keller and Pinter, 2002), and the hypsometric curve (*HC*) elucidate the erosion and sedimentation dynamics within a drainage basin and are thereby interlinked with its tectonic evolution and geomorphological characteristics (Pike and Wilson, 1971; Keller and Pinter, 2002). The *HI* index delineates the elevation distribution across a defined region within the drainage basin. It is quantified as the area beneath the *HC*, which encapsulates the cumulative volume of the uneroded basin.

$$HI = \frac{h_{mean} - h_{min}}{h_{max} - h_{min}} \tag{4}$$

where *HI* denotes the hypsometric integral, h_{mean} is the mean elevation

Table 1
Mean morphometric characteristics of mountain fronts and drainage basins within the Pütürge segment.

Geomorphic Features	Pütürge Segment of the EAFS			
	S1	S2	S3	S4
Number of valleys	5	2	1	2
Mountain front sinuosity (Smf)(1)	1.3	1.6	1.3	1.5
Valley Floor width-to-height ratio (Vf)(2)	0.52	0.42	0.71	0.30
Asymmetry factor (AF)(3)	45	36	48	55
Hypsometric integral (HI)(4)	0.46	0.46	0.54	0.47
Drainage basin shape (Bs)(5)	3.47	3.12	3.12	3.39
Normalized Steepnes Index (ksn)(6)	96.4	140	125	98.5
Gilbert metric and Chi (χ)(7)	Movement to SW		Stable	

of the basin, h_{min} represents the minimum elevation of the basin and h_{max} is the maximum elevation of the basin.

Hypsometric curves are graphical depictions derived by plotting the cumulative elevation ratio of the basin against the cumulative basin area ratio. The configuration of the hypsometric curve facilitates the determination of various developmental stages of the basin, ranging from mature (more developed) to youthful (less developed) phases.

(5) Drainage basin shape (***Bs***)

In regions marked by active tectonics, drainage basins typically exhibit an elongated configuration, gradually transitioning toward a more circular shape over time due to topographic evolution or a decrease in tectonic activity (Bull and McFadden, 1977). The drainage basin shape (*Bs*) is determined by equation (5) (Cannon, 1976).

$$Bs = \frac{Bl}{Bw} \tag{5}$$

where *Bl* is the basin's length, and *Bw* denotes the width of the basin.

Basins with elongated geometries generally yield higher *Bs* values mainly due to heightened tectonic activity, whereas circular basins, clearly indicative of minimal tectonic influence, typically yield lower *Bs* values. Consequently, *Bs* values serve as a diagnostic tool for evaluating the degree of tectonic activity within a given basin.

(6) Normalized steepness index (***ksn***)

The normalized channel steepness index or simply normalized steepness index (*ksn*) is an invaluable tool for delineating the spatial distribution of intracontinental deformation and documenting the history of regional uplift. The *ksn* has been employed to calculate the changes in vertical tectonic deformation at strike-slip fault zones in various regions of the Earth, such as the Haiyuan Fault in China (Li et al., 2019), the Altyn Tagh Fault in China (Wang et al., 2019), the Owen-Stanley Fault Zone in Oceania (Sun and Mann, 2021), the Ovacık Fault in Eastern Türkiye (Yazıcı et al., 2018) and the Malatya Fault in Eastern Türkiye (Zabcı, 2020).

Analyses of bedrock river profiles give rise to essential data on a region's lithological composition, tectonic history, and past climatic conditions, all of which are subject to thorough examination (Kirby and Whipple, 2001, 2012). The bedrock profiles are predicated upon the stream power erosion model, articulated in equation (6) as follows (Whipple and Tucker, 1999):

$$\frac{d_z}{d_t} = U - KA^m S^n \tag{6}$$

where *U*, *A*, and *S* denote the bedrock uplift rate, catchment area, and channel slope, respectively; *K* represents a constant contingent upon rock erodibility, precipitation patterns, and channel geometry; *z* signifies the elevation of a point within the channel; *t* denotes time; and *m* and *n* are empirical parameters. This equation is universally used for any erosion law involving power law scaling between channel slopes and drainage areas under steady-state conditions (Willett et al., 2014). If *U* and *K* exhibit spatial and temporal constancy, the steady-state solution of this problem can be expressed in equation (7), as elucidated by Perron and Royden (2013):

$$z(x) = z_b + \left(\frac{U}{KA_0{}^m}\right)^{\frac{1}{n}} \chi \tag{7}$$

where $z(x)$ represents the elevation of a point within the channel, z_b is the elevation of the base level, and A_0 is the reference drainage area. χ, representing an integral function of the position within the channel network, can be mathematically expressed as in equation (8):

$$\chi = \int_{x_b}^{x} \left(\frac{A_0}{A(x')}\right)^{\frac{m}{n}} d_{x'} \tag{8}$$

In this computational pattern, *z* is represented along the vertical axis, while χ is depicted along the horizontal axis, constituting what is commonly referred to as the χ-plot (Perron and Royden, 2013). Consequently, the χ-plot serves as a frequently employed tool for deducing the regional relative bedrock uplift rate (Gallen and Wegmann, 2017).

(7) Gilbert metrics and Chi (χ)

χ is one of the pivotal parameters utilized in delineating cleavage migration (Willet et al. 2014). Interpretations of χ anomalies require an assumption of comparable rock elevation, strength, and climatic conditions (Whipple et al., 2017). Consequently, disparate χ values may denote varying migration directions (Forte and Whipple, 2018; Whipple et al., 2017). To address this challenge, the Gilbert metric, which was initially proposed by Gilbert (1987) and later refined by Whipple et al. (2017), was introduced. Previous research has suggested that the amalgamation of Gilbert metrics and disparities in χ along the watershed divide can effectively delineate the divide's present and potential migration directions in contemporary applications (Forte and Whipple, 2018; Whipple et al., 2017). While χ furnishes insights into the prospective evolution of the drainage basin, the Gilbert metrics depict its current state (Forte and Whipple, 2018).

3.3. Analyzing the velocity distribution and slip rates with remote sensing data

A satellite navigation system operates by using satellites for geopositioning. Global navigation satellite systems (GNSS) provide worldwide coverage through interconnected satellite networks. GPS systems are the most commonly used GNSS applications. GNSS data enables ground velocity modeling, which is particularly crucial in seismically active regions dominated by plate tectonics. A receiver determines its location within meters by measuring signal travel time from visible satellites. This method tracks relative displacement changes between stationary and moving areas over time. Each observation point yields displacement velocity in mm per year, with more points enabling more precise relative motion modeling. GNSS-based models characterize regional deformation through velocity magnitude, direction, and orientation. Continental interpretations from GNSS data assume stable plate regions and elastic-rebound theory between plates.

Unfortunately, only a few research studies (e.g., McClusky et al., 2000; Reilinger et al., 2006; Kreemer et al., 2014; Kurt et al., 2023) fully include Türkiye in terms of geographical coverage. Generally, GNSS-based studies progress by revising and enriching the data from previous studies, which enables us to understand better the motion behavior of the area examined over a particular timeframe as new studies emerge. Since the publication dates of these studies were spread apart and their scope continued to expand, the velocity field and strain rate data from Reilinger et al. (2006) and Kurt (2023) were reprocessed, and velocity distribution maps were drawn for a part of East Anatolia covering the study area. In particular, the study by Kurt et al. (2023) is the most comprehensive study ever conducted for Türkiye in recent years, utilizing the latest state-of-the-art techniques and covering a long timeframe. The method provided excellent spatial coverage for our study and comparison of our findings. Furthermore, from Bilham et al. (2023), creepmeter measurements made after February 6, 2023, earthquakes in certain areas within the study area of the present article were re-digitized and compared with known velocity models to understand the formation process of the earthquakes along with active deformation, particularly after the February 6 earthquakes.

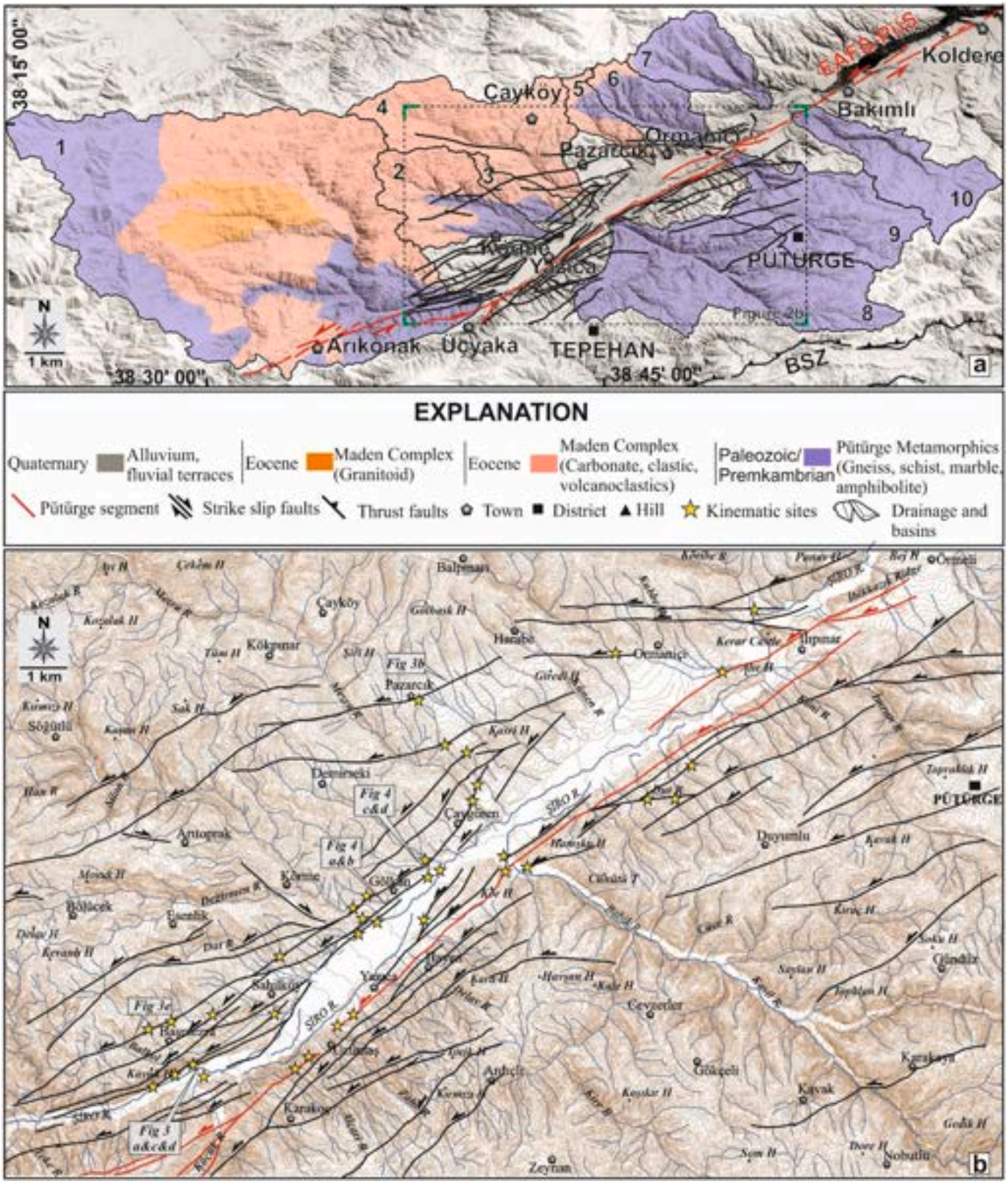

Fig. 2. (a) The distributions of the geological units (Akbaş et al., 2011) along the drainage basins on the DEM (USGS) (The dark area in the upper-right corner represents the course of the Fırat River) and (b) the fault geometry of the Pütürge segment on a topographic map with a 1:25,000 scale.

4. Results

4.1. Kinematic analysis

Seventy-nine fault slip data points were measured from 15 sites on the north and south sides of the Şiro Valley (Fig. 2b). These measurements were obtained from the units lying along the fault zone to investigate the kinematic history and present-day stress conditions of the Pütürge segment along the EAFS (Fig. 2a). Kinematic analysis was carried out based on the deformation ellipsoid, considering the ~N60°E trend of the Pütürge segment. The measured data were classified according to their pitch. The results of the kinematic analysis, presented in Table 2, reveal three distinct stress regimes. All kinematic sites except for two locations (PS-5 and PS-7) indicate strike-slip deformation of the EAFS and extensional deformation compatible with this strike-slip regime.

Fault slip data from kinematic sites PS-1 and PS-7 suggest a compressional stress tensor with a vertical σ3. The compressive stress tensors represent pure compressional (PS-7) and transpressional (PS-1) tectonic regimes, determined by the stress ratio (R) and stress regime index (R′) values. Kinematic sites exhibiting purely compressional tectonic regimes with a maximum stress axis direction (σ1) oriented NNE–SSW and transpressional tectonic regimes with a minimum stress axis direction (σ3) oriented NW–SE affect the schists of the Upper Paleozoic Pütürge Metamorphics. PS-7, which exhibits a purely compressional tectonic regime, was found to have developed under a stress state in an approximately N–S direction. This site reflects the prevailing stress state before the formation of the EAFS and is associated with the continental collision between the Arabian and Anatolian plates. The transpressional tectonic regime in the extensional stress regime, with an approximately NW–SE orientation at site PS-1, was caused by the deformation of the EAFS.

Fault slip data from kinematic sites PS-2A, PS-4, PS-8, and PS-9 indicate a strike-slip stress tensor with vertical σ2. These sites are characterized by strike-slip regime indexes (PS-2A, 4, and 8) and a transtensional regime index (PS-9), as determined by the calculated stress ratio (R) and stress regime index (R′). The maximum stress axes (σ1) for these sites are oriented NNE–SSW (PS-4 and 9) and NE–SW (PS-2A and 8), which deform both schists of the Upper Paleozoic Pütürge Metamorphics and Middle Eocene Maden Complex olistoliths, respectively. Principally, these sites exhibit sets of striking and subparallel faults with low pitch angles, reflecting the dominant strike-slip nature of the EAFS (Fig. 3a–c & d). Additionally, shear zones are observed on the outcrops along the Pütürge segment based on the fault geometry (Fig. 3e).

Fault slip data from kinematic sites PS-2B, 3, 5, 6, 10, 11, 12, 13, 14, and 15 indicate an extensional stress tensor with a vertical σ1. These sites exhibit variations in extensional regimes, ranging from extension (PS-3, 5, 6, 12, 13) to transtensional (PS-2B, 14, 15) and radial extensional (PS-10, 11) styles, as determined by the calculated stress ratio (R) and stress regime index (R′). Notably, the minimum stress axis (σ3) orientation (NE–SW) at site PS-5, measured within the Upper Paleozoic schists, is not in harmony with the expected deformation pattern of the EAFS. Kinematic analysis of fault slip data from all other sites suggests that the extensional tectonic regime, characterized by a minimum stress axis (σ3) oriented NW–SE, affected the Upper Paleozoic Pütürge Metamorphics and the Middle Eocene Maden Complex units. This extensional regime, represented by high pitch angles (Fig. 3b), is consistent with the overall deformation pattern and geometry of the Pütürge segment along the EAFS.

4.2. Morphometric analysis

4.2.1. Mountain front sinuosity index (*Smf*)

Smf values were computed for the mountain fronts adjacent to faults in the Şiro Valley. Calculations were conducted across four delineated regions along the northern and southern mountain fronts, revealing *Smf* values ranging from 1.3 to 1.6. Areas designated 1 and 3 yielded the lowest *Smf* values, while the highest *Smf* value was recorded in area 2 (refer to Table 3 and Fig. 4). The relatively diminished *Smf* values observed in areas 1 and 3 suggest a comparatively flatter terrain profile compared to the other regions. By employing the classification system proposed by El-Hamdouni et al. (2008), the outcomes were categorized into three distinct classes: class 1 (high), ranging from 1 to 1.5; class 2 (moderate), spanning from 1.5 to 2.5; and class 3 (low), exceeding 2.5. Notably, the data revealed an absence of values falling within the lowest class in the mountain block under investigation.

4.2.2. Valley floor width–valley height ratio (*Vf*)

The *Vf* values were calculated to elucidate the geometric attributes of the drainage basins. The *Vf* values were determined using transverse valley profiles located approximately 800 m above the mountain fronts (see Fig. 4). The *Vf* values ranged from 0.29 to 0.71, with the minimum observed in drainage area 7 and the maximum in drainage area 8 (refer to Table 3). Drainage areas 2, 3, 7, 9, and 10 exhibited a "V-shaped" geometry, while drainage areas 1, 4, 5, 6, and 8 manifested a "U-shaped" geometry. Following the classification system proposed by El-Hamdouni et al. (2008), the *Vf* values are categorized into three classes: class 1 (*Vf*

Table 2
Calculations of kinematic analysis of fault slip data measured from the Pütürge segment along the Şiro Valley (PS-1/4/5/6/7/9/11/13/14 and 15 denote the majority of the schist and amphibolite lithology within the Pütürge Metamorphics, respectively; PS-2A/2B/3/8/and 10 depict the olistolith lithology within the Maden complex).

Location	Longitude	Latitude	N	σ_1	σ_2	σ_3	R	R'	TR	α
PS-1	38.776120°	38.228226°	3	25/013	27/270	52/139	0.17	2.17	TP	15.4
PS-2A	38.737999°	38.207990°	4	04/050	66/241	04/142	0.50	1.50	SS	1.6
PS-2B	38.737999°	38.207990°	4	74/217	14/008	07/100	0.75	0.75	TT	10.2
PS-3	38.729043°	38.220080°	10	68/188	20/034	09/301	0.51	0.51	PE	11.3
PS-4	38.718655°	38.181688°	5	01/184	66/277	24/094	0.71	1.29	SS	5.4
PS-5	38.714312°	38.179368°	4	73/138	15/349	08/257	0.36	0.36	PE	11.2
PS-6	38.694703°	38.169566°	3	54/023	36/208	03/116	0.50	0.50	PE	5.6
PS-7	38.676648°	38.157165°	4	05/185	09/094	80/300	0.58	2.58	PC	7.2
PS-8	38.662869°	38.155383°	6	27/223	50/096	27/238	0.46	1,54	SS	4
PS-9	38.672189°	38.147812°	11	25/010	60/155	15/273	0.77	1,23	TT	14.3
PS-10	38.669216°	38.146682°	5	77/002	09/230	09/139	0.10	0.10	RE	4.1
PS-11	38.668038°	38.136340°	2	69/027	18/236	10/143	0	0	RE	15.6
PS-12	38.697817°	38.146679°	3	73/171	13/032	11/300	0.50	0.50	PE	12.4
PS-13	38.755280°	38.186303°	4	76/086	10/222	10/314	0.67	0.67	PE	6.1
PS-14	38.785995°	38.201160°	7	90/000	00/190	00/100	0.86	0.86	TT	14.5
PS-15	38.785555°	38.200045°	4	81/220	08/014	04/104	0.76	0.76	TT	5.2

N: Number of measurements, D: Direction, P: Plunge, σ1, σ2, σ3: principal stresses (σ1 > σ2 > σ3), R: Stress ratio, R': Stress regime index, TP: Transpressional, SS: Pure Strike-Slip, TT: Transtensional, PE: Pure Extensional, PC: Pure Compressive, RE: Radial Extensional, α: Misfit angle.

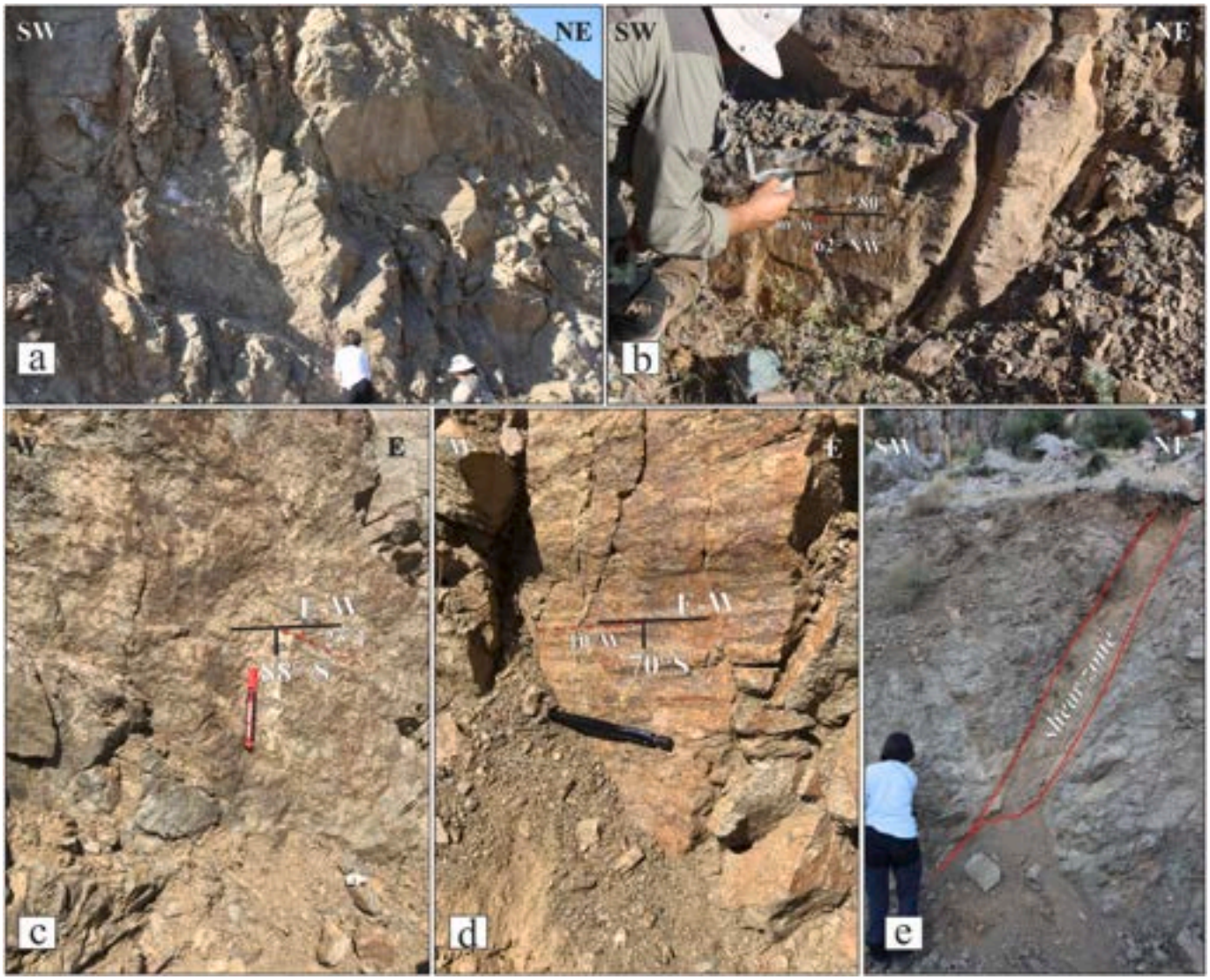

Fig. 3. Outcrop (a&e) and fault plane (b, c, d) views of the Pütürge segment with the fault slip data observed in the basement rocks along the northern and southern edges of the Şiro Valley.

Table 3
Morphometric parameters derived for the Şiro Valley.

Drainage Number	Total Area (km^2)	Smf/C		Vf/C		AF/C		Hi/C		Bs/C		Ksn/C		Iat/C
1	308	1.3	1	0.54	2	69	1	0.47	2	1.94	3	87	2	2-H
2	40			0.34	1	56	3	0.45	2	3.74	2	100	2	2-H
3	11			0.39	1	24	1	0.32	1	3.76	2	57	3	1-VH
4	58			0.69	2	33	1	0.65	3	2.94	3	120	2	2-H
5	12			0.63	2	43	2	0.43	2	4.99	1	118	2	2-H
6	20	1.6	2	0.55	2	30	1	0.41	2	3.81	2	120	2	2-H
7	27			0.29	1	41	2	0.51	1	2.43	3	160	1	2-H
8	94	1.3	1	0.71	2	48	3	0.54	1	3.12	2	125	2	2-H
9	51	1.5	1	0.24	1	65	2	0.53	1	2.36	3	105	2	2-H
10	38			0.35	1	44	3	0.41	2	4.42	1	92	2	2-H

≤ 0.5), class 2 ($0.5 \leq Vf < 1$), and class 3 ($Vf \geq 1$). As depicted in Table Z, the mean *Vf* values of the drainage basins align with those of class 2.

4.2.3. Asymmetry factor (AF)

The *AF* index, utilized to assess tilting and relative tectonic uplift within drainage areas, was computed for all ten delineated drainage areas. The calculated values ranged from 24 to 69, with higher values indicating tilting toward the southwest while lower values indicating tilting toward the northeast (see Table 3 and Fig. 4). The results reveal that 70% of the *AF* values exhibit an asymmetrical basin pattern, while 30% reflect a symmetrical basin configuration. Following the classification standard suggested by El Hamdouni et al. (2008), the *AF* results are categorized into three different classes: class 1 ($AF \leq 35$), class 2 ($57 \leq AF < 65$ or $35 \leq AF < 43$), and class 3 ($43 \leq AF < 57$).

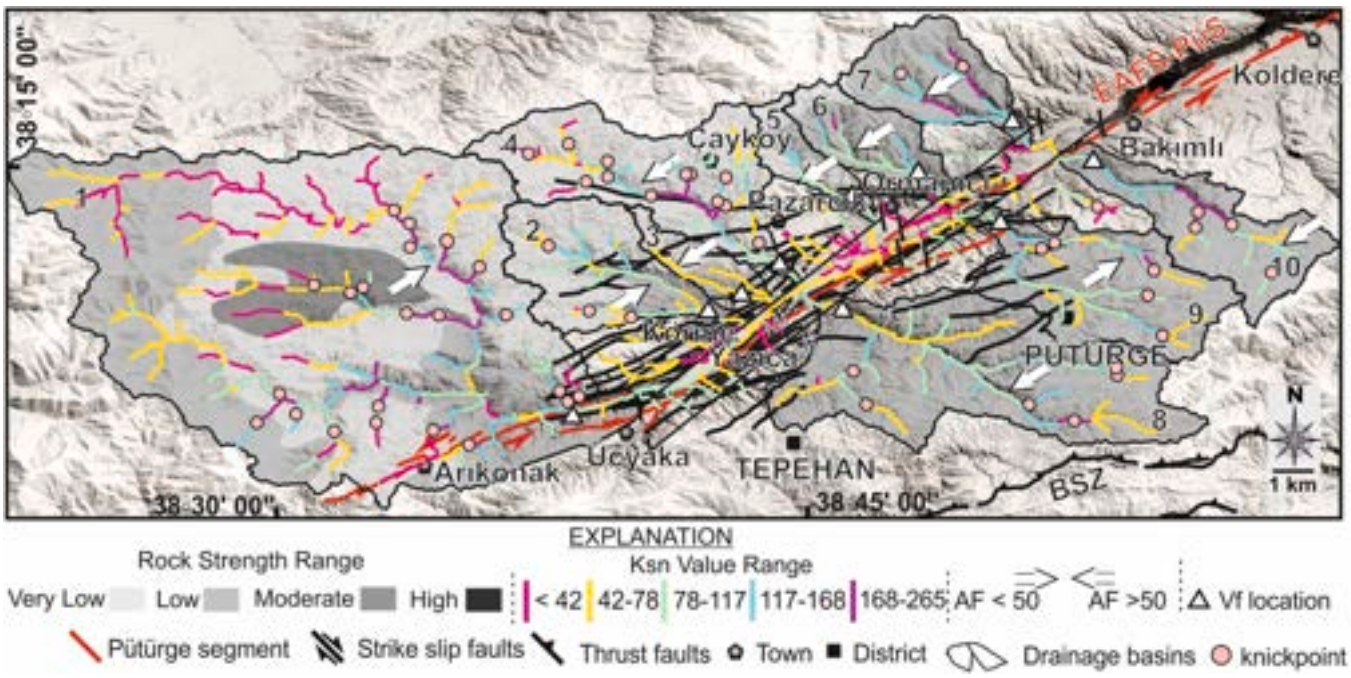

Fig. 4. Representation of the morphometric indices applied along the main river branches of the drainage basins created throughout the Şiro Valley on the digital elevation model. ksn: normalized steepness index with knick points (KP), Bs: basin shape geometry, Vf: ratio of valley floor width to height, Smf: mountain front curvature, EAFSZ-PüS: East Anatolian Fault System-Pütürge Segment, BSZ: Bitlis Suture Zone (The dark area in the upper-right corner represents the course of the Fırat River).

4.2.4. Hypsometric integral and curve (*HI* and *HC*)

The *HI* and *HC* serve as analytical tools to explore the quantitative relationship between the area and elevation of the horizontal section of a drainage basin. They aid in assessing basin development stages by providing insights into the basin's geomorphic evolution and landscape characteristics. In this manner, *HI* values were computed for each drainage basin within the study region (refer to Table 3), and *HC* curves were plotted (see Fig. 4). Analysis of these curves suggests that drainage area 4 in the northern part of the basin exhibits characteristics of a young basin, while drainage area 3 indicates a mature stage. Conversely, *HC* analysis suggested that drainage areas 8, 9, and 10 appear to be in the mature stage based on HI analysis. The computed *HI* values were classified into three categories according to the criteria given by El-Hamdouni et al. (2008). Class 1 ($HI \geq 0.5$) corresponds to convex hypsometric curves, class 2 ($0.4 \leq HI < 0.5$) corresponds to concavo-convex or flat S curves, and class 3 ($HI \leq 0.4$) represents concave profiles. Overall, 40% of the *HC* profiles exhibit convex shapes, 10% are concave, and the remaining 50% exhibit flat S curves.

4.2.5. Drainage basin shape (*Bs*)

The *Bs* index (e.g., circularity ratio or elongation ratio) was employed to investigate alterations in the shape of drainage basins induced by tectonic movements within the study area. The *Bs* values ranged from 1.94 to 4.99 (Table 3). The data analysis revealed that drainage areas 1, 4, 7, and 9 exhibited an elongated basin morphology, whereas areas 2, 3, 5, 6, 8, and 10 demonstrated a circular basin morphology. Following the classification system proposed by Ellias (2015), the obtained *Bs* values were classified into three distinct classes. Class 1 ($Bs \geq 4$) designates elongated basins, class 2 ($3 \leq Bs < 4$) denotes semi-elongated basins, and class 3 ($Bs \leq 3$) signifies circular basins.

4.2.6. Normalized steepness index (*ksn*)

The *ksn* index was computed for the ten drainage basins to assess channel steepness and its potential correlation with tectonic activity. The calculated average *ksn* values ranged from 57 to 160. Noticeably, the *ksn* values tended to be higher near faults, particularly in upstream regions (see Fig. 4), where the distribution of knickpoints generally aligned with areas characterized by high *ksn* values. Moreover, *ksn* profiles delineated fluctuations in channel steepness along each river profile. In certain regions, these variations corresponded to faulting activities, while in others, they signified abrupt changes in terrain steepness, such as the presence of waterfalls (see Fig. 4). Furthermore, the *ksn* values were further stratified into three distinct classes: class 1 denoted high values ($ksn \geq 150$), class 2 represented average values ($80 \leq ksn < 150$), and class 3 indicated low values ($ksn \leq 80$). Subsequently, an evaluation of the *ksn* values for all the obtained basins suggested a transition toward class 2, manifesting moderate tectonic activity.

4.2.7. Gilbert metrics and χ

Notable variations and contrasts are observed in the χ maps (refer to Fig. 5) generated for the study area, particularly within drainage area 1. This observation is substantiated by Gilbert metric computations, which suggest a trend toward southward migration.

The primary drainage network was divided into three distinct sections (D1, D2, and D3) for the northern regions to assess segmental migration, while a single segment (D4) was delineated for the southern regions (see Fig. 5). Subsequent computations of the Gilbert metrics and χ values revealed that segments D1 and D2 exhibit instability, suggesting potential southward migration. Conversely, all segments, except D1 and D2, demonstrated stability in their Gilbert metric profiles (see Fig. 6). Segment D1 encompasses drainage areas 1, 2, and 3, coinciding with the vicinity of the graben boundaries of the main faults. It is quite conceivable that tectonic activity, specifically movement along faults, which contributes to southward migration, could intensify uplift in this region, potentially resulting in the southward displacement of the central segment lineament.

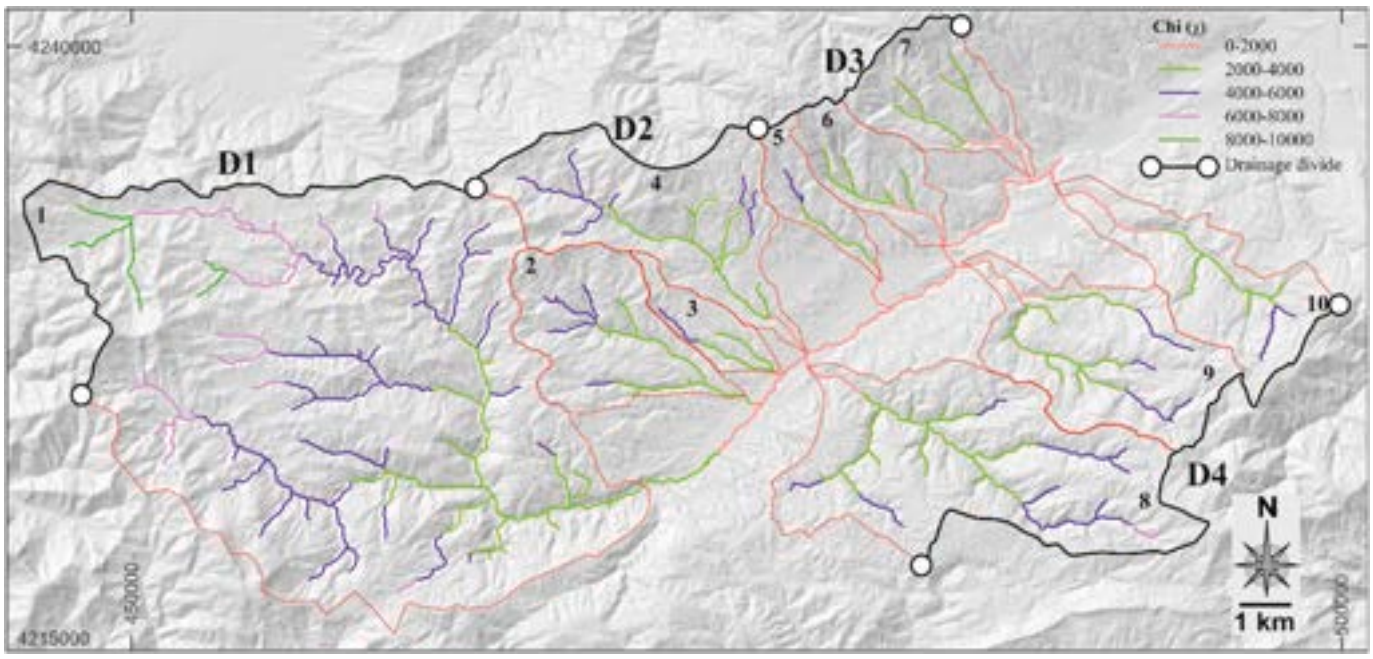

Fig. 5. χ map of the Şiro Valley.

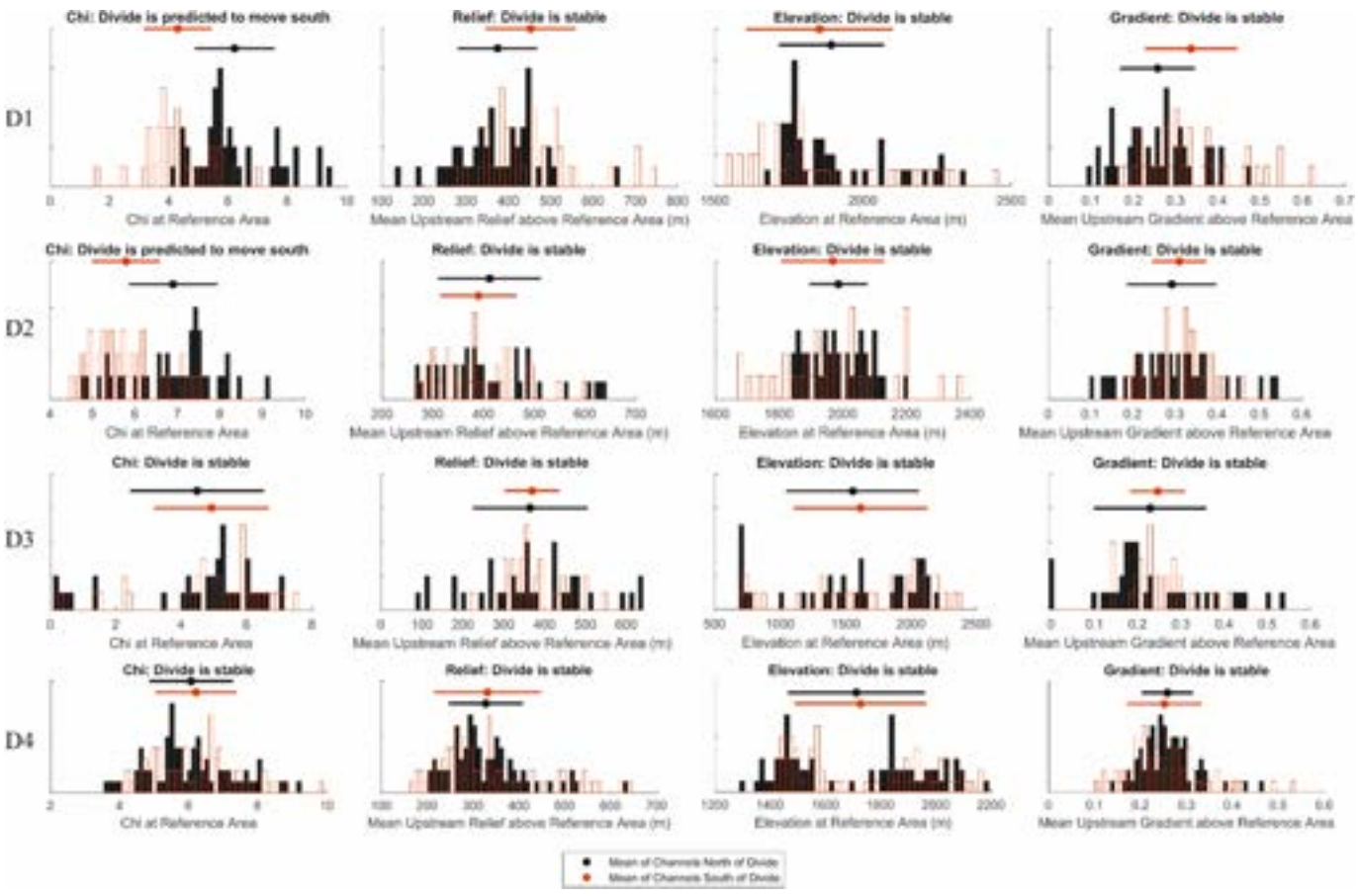

Fig. 6. Histograms of the divide metrics (Gilbert metrics and χ) for the D1, D2, D3 and D4 segments (histograms with white–red rectangles represent drainage basins in the north, while histograms with black fills represent drainage basins in the south). All calculations for the Gilbert metrics and χ were determined starting from the 1000 m elevation level). (For interpretation of the references to color in this figure legend, the reader is referred to the Web version of this article.)

5. Discussion

5.1. On the existing stress distribution along the Pütürge segment of the EAFS

This section discusses the stress distribution along the Pütürge segment of the East Anatolian Fault System (EAFS). The Pütürge segment branches out extensively in the southwestern part of Hazar Lake, forming a stepped morphology and a wide deformation zone. This zone continues toward the Euphrates River valley, creating deep canyons by merging fault branches and thereby developing a narrow deformation zone. The Pütürge segment, identified as the asymmetrical counterpart of Hazar Lake, exhibits a wide deformation zone as it branches again in the Şiro Valley from the Euphrates River valley. In areas where the deformation zone expands, faults become more parallel and exhibit significant normal components, indicating an oblique-slip faulting mechanism. This extensional tectonic regime, acting alongside the strike-slip regime, has led to the development of stepped morphology in these areas (Çetin and Güneyli, 2002; Akgün and İnceöz, 2021).

Fig. 7 presents fault-plane solutions retrieved from the hub of the Disaster and Emergency Management Presidency of Türkiye (AFAD) (https://deprem.afad.gov.tr/event-focal-mechanism), categorized using earthquakes that occurred in the East Anatolia region and for which focal mechanisms were resolved. Additionally, Fig. 7 b displays fault solutions for earthquakes specifically occurring within the capture basins examined in this study and their vicinity. Accordingly, while the major earthquakes (Mw $\geq$ 5.0) in the main branches of the EAFS are left-lateral strike-slip earthquakes in accordance with the main characteristics of the NW dipping fault (Eyidoğan, 2021), others also exhibit normal components within the fault and its nearby branches. InSAR analyses of Sentinel-1 data following the 2020 Sivrice-Doğanyol earthquake revealed vertical displacements ranging from −19 cm in the northeastern part to 32 cm in the southwestern part of the Pütürge--Doğanyol (Malatya) settlements (Karslıoğlu et al., 2021). While the significant vertical displacement in the southwestern region and the

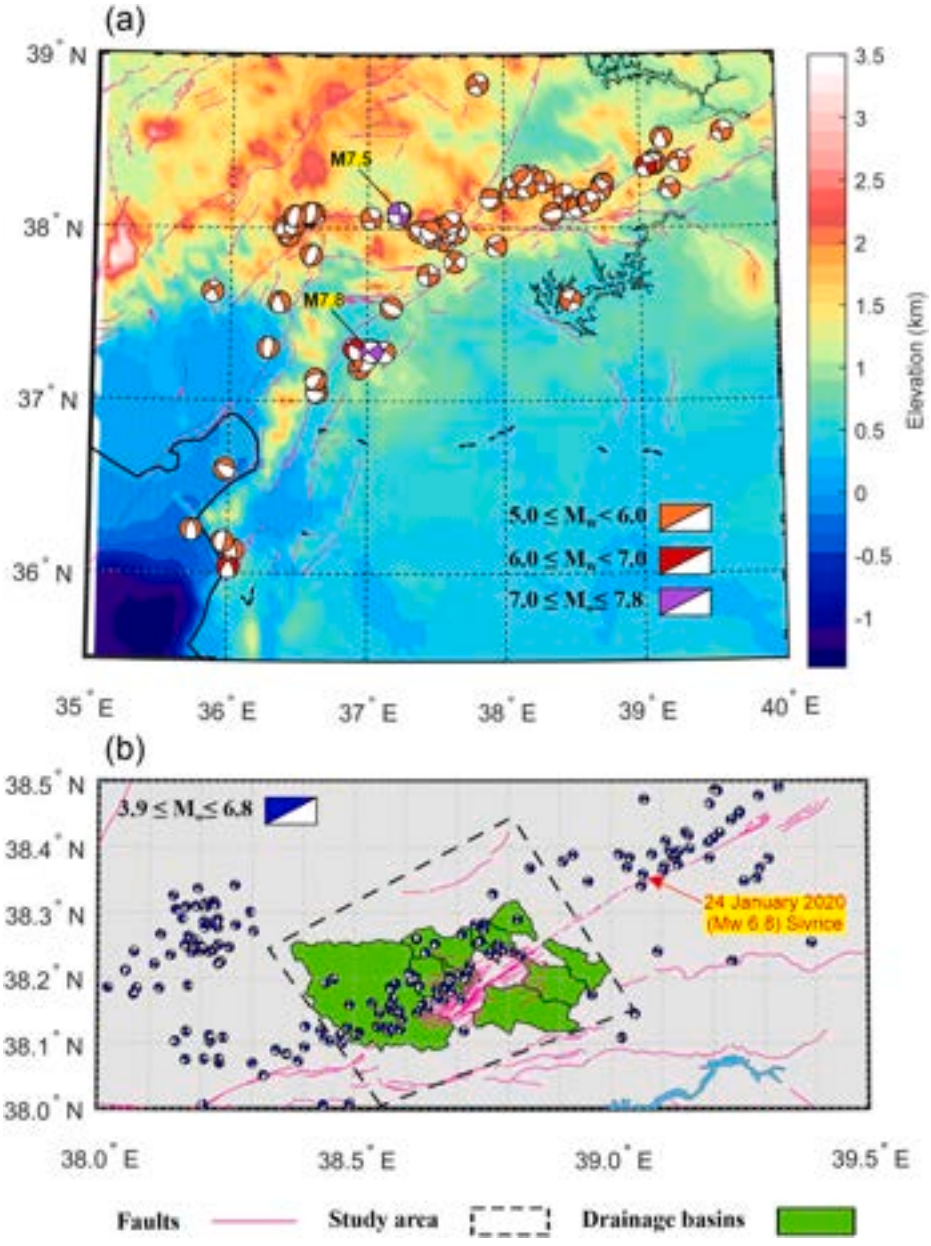

Fig. 7. Maps of the fault-plane solutions; a for all ranges of the EAFS, b for the study area that covers the drainage basins resting in the Şiro Valley.

observed subsidence are lithologically related (Karslıoğlu et al., 2021), these findings also align with the geometry and transtensional kinematic behavior of the Pütürge segment along the Şiro Valley. By examining the study area and the identified basins more closely in Fig. 7 b, it can be seen that the earthquake frequency is greater in the basins in the western direction of the valley. In addition, in this article, earthquakes occurred on new faults that moved along the valley bottom line and into the basins. This is an excellent example of the fact that essentially unmapped areas still exist in the region. In parallel, Fig. 7b clearly shows that there is a persistent earthquake cluster in an area that is not on the active fault map between 38° and 35°E. Although this area is beyond the scope of this study, it indicates that many active faults or fault mechanisms in the region are waiting to be identified.

The Şiro Valley is not limited by fault control on its southern edge, as depicted in the active fault map (Duman and Emre, 2013). However, both sides of the valley are faulted, forming a broad strike-slip shear zone with a normal component. Like Hazar Lake, the Şiro Valley presents a topography with steeper slopes along the southern edge and gentler slopes along the northern edge, likely due to the varying distances from faults (Çetin and Güneyli, 2002; Çetin et al., 2003). Left lateral deformation and the accompanying dip-slip movement mechanism were observed morphologically along the Pütürge segment. Several geological structures throughout the Pütürge segment characterize sinistral deformation. These include alluvial fans that developed under fault control, elongated ridges that developed parallel to the fault, left-lateral offsets in drainages, cut triangular surfaces, and fault-controlled stream terraces (Fig. 8).

Apart from the different stream terrace levels elevated by the Pütürge segment around the Şiro Valley, there are generally metamorphic and complex basement units throughout the valley. Analysis of fault data from the northern and southern edges of the Şiro Valley reveals a strike-slip stress regime with coexisting extensional tectonics within the Pütürge segment of the EAFS. The deformation zone widens as the segment branches again in the Şiro Valley from the Euphrates River valley. Furthermore, Lyberis et al. (1992) mapped the NW-trending conjugate fault sets crossing the Şiro Valley along the Pütürge segment using satellite imagery. Stream terrace levels controlled by the branches of the Pütürge segment along the Şiro Valley

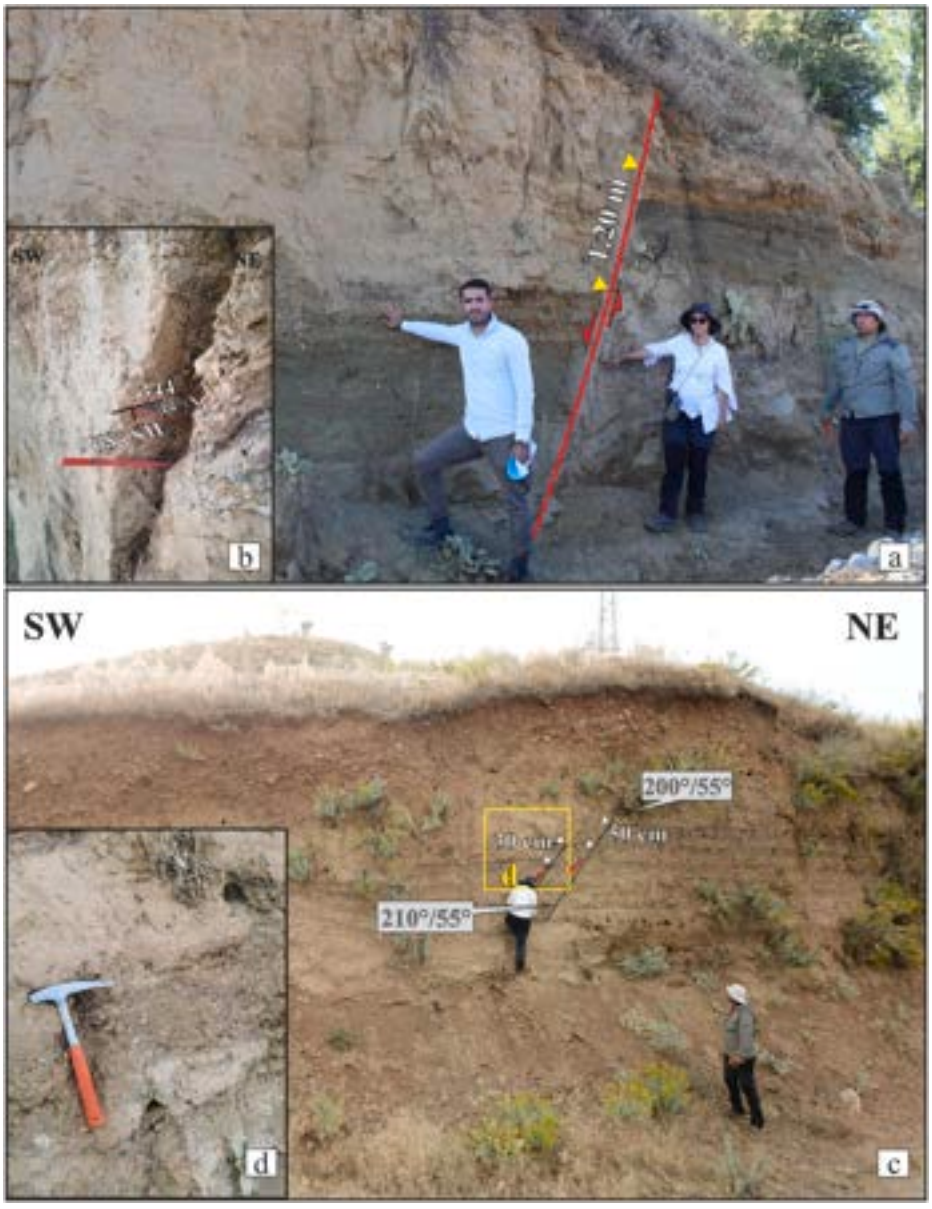

Fig. 8. Faulting view of the T1 terrace-level fault plane with fault striations in the southwestern Gölkan (a&b) and Çaygören (c&d) on the northern coast of the Şiro Valley. Offsets at terraces deformed by the Pütürge segment.

are deformed by NW-oriented conjugate faults with vertical displacements of up to approximately 1 m (Fig. 8 ab), demonstrating the tectonic activity of the segment. The 35° pitch angle indicates a strike-slip-dominated character with a normal faulting component (Fig. 8b). Specifically, the elevation difference at river terrace levels is influenced by the development of normal faults due to the extensional tectonic regime (Fig. 8).

The transtensional tectonic regime accompanying the recent strike-slip deformation aligns with paleostress results and stress states reported by Akgün and İnceöz (2021). Furthermore, the stress directions and tectonic regimes calculated based on the focal mechanism solutions of the earthquakes indicate active strike-slip tectonics (R': 1.42–1.51 ± 0.28) with a maximum horizontal stress-oriented NNE–SSW (S_{Hmax}: N20°-28°E±13.1°) throughout the Pütürge segment (Akgün, 2021; Harzali et al., 2023). The kinematic analysis of the extensional and conjugate structural elements accompanying the main fault in the left lateral deformation model reveals various tectonic regimes, including purely strike-slip, purely extensional, radially extensional, transtensional, and transpressional regime indexes with NNE–SSW S_{Hmax} and NW–SE S_{Hmin} throughout the Şiro Valley. These kinematic sites depict the recent deformation phase of the extensional tectonic regime associated with the strike-slip tectonic regime along the Şiro Valley (Fig. 9). Kinematic analysis at several locations (PS-5 and PS-7) suggested deformation from ancient periods. These kinematic locations reflecting

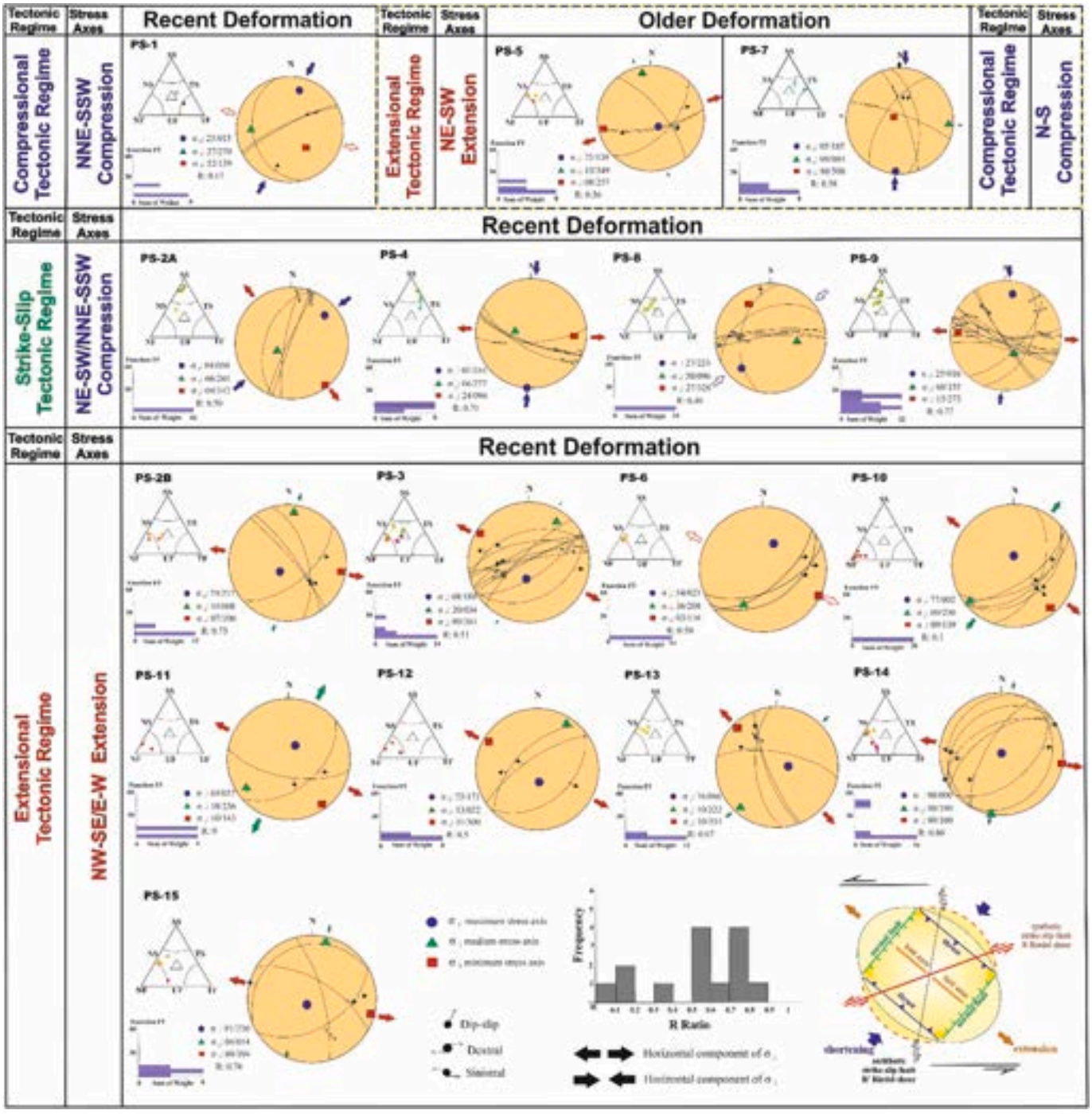

Fig. 9. Representation of the lower hemisphere stereo plots of the analysis of kinematic data associated with the measured deformation of the Pütürge segment along the Şiro Valley and schematic view of the left lateral deformation ellipsoid.

different phases under the influence of compressional and extensional stress states in different directions have been compared and associated with studies that reveal the regional stress states and plate motion relationships suggested for the Eastern Mediterranean (Şengör et al., 1985; Dercourt et al., 1986; Muehlberger and Gordon, 1987; Lyberis et al., 1992; Herece, 2008; Kaymakçı et al., 2010). The NE–SW extensional regime is associated with Paleocene basins formed by rapid uplift and erosion following subduction in the Maastrichtian period (Fig. 9). The NE–SW extensional regime observed at PS-5, based on kinematic data from Paleozoic schists, is characteristic of the Maastrichtian phase (Herece, 2008), which was identified as the earliest tectonic phase (Kaymakçı et al., 2010).

Paleozoic-Mesozoic-aged metamorphic units within the study area were pushed onto the Miocene basin by thrust faults due to N–S trending maximum horizontal stress that started during the late Serravalian period (Herece, 2008). This compressional regime reflects the closure of the Neotethys Ocean and the onset of continental collision, leading to E-W-trending reverse faults and fold axes in the Eastern Mediterranean (Fig. 9). In addition to thrust and fold formations during this deformation phase, where the convergence between the Arabian and Eurasian plates changes in a counterclockwise manner (Navabpour et al., 2007), the deformation is also related to conjugate strike-slip faults and oblique faults with reverse components (Herece, 2008). The N–S compressional regime observed at PS-7, based on kinematic data from Paleozoic schists, is characteristic of the middle-late Miocene phase (Herece, 2008), which was identified as the fourth tectonic phase (Kaymakçı et al., 2010).

5.2. *The relative tectonic activity of the Pütürge segment in the Şiro Valley*

Morphometric indices serve as valuable instruments for assessing relative tectonic activity, particularly in regions with limited investigations into tectonic dynamics, such as the Pütürge segment of the EAFS. Nonetheless, it is crucial to recognize that these indices are prone to the influence of various external factors, potentially leading to misinterpretations and ambiguous tectonic analyses (Keller and Pinter, 2002; Kirby and Whipple, 2012). Notably, climate emerges as one of the foremost elements exerting control over erosion rates, thereby significantly influencing landscape evolution (Whipple, 2009).

Within the active orogenic regions of East Anatolia, climate-driven denudation has emerged as a notable external mechanism that promotes surface uplift over short timescales, primarily driven by rapid fluvial discharge (Cederbom et al., 2004; Menéndez et al., 2008; Whipple, 2009). This intricate interplay between climate dynamics and erosion rates profoundly influences the configuration of river profiles and the adjustment of drainage systems within newly established equilibrium (or disequilibrium) states. Consequently, this process governs the overall topographic relief and dreinage asymmetry observed within active tectonic regions (Willett, 1999; Roe et al., 2003).

Lithological disparities can significantly impact landscape and river profiles, as pronounced variations in bedrock erodibility exert a profound influence on geomorphic indices associated with incision patterns, such as the *ksn* index (Whipple and Tucker, 1999; Kirby and Whipple, 2001; Whittaker et al., 2008). Furthermore, these disparities may also alter analyses of the χ index in divide migration analysis (Forte and Whipple, 2018a). In that sense, the drainage basin situated along the Pütürge segment provides an exceptional opportunity for rigorous geomorphological analysis.

In this investigation, we employed Selby's (1980) rock strength scales, following methodologies similar to those used in prior studies (e.g., El Hamdouni et al., 2008; Alipoor et al., 2011; Topal et al., 2016; Softa et al., 2018; Softa, 2022), which are based on the rock unit and cementation type, thus highlighting that rocks are more resistant to weathering and fluvial erosion. The classification of rock strength encompasses categories ranging from very low (e.g., alluvium, terraces) to low (e.g., conglomerate, sandstone, claystone), moderate (e.g., mélange deposits), and high (e.g., gabbro and metamorphics).

The Pütürge segment comprises a diverse array of rock formations, including Paleozoic intrusive structures, Paleozoic-Mesozoic Puturge Metamorphics, Middle Eocene Maden melange, Miocene clastic deposits, and Plio-Quaternary terraces and alluvium. In particular, sharp spikes in *ksn* values are readily discernible within regions characterized by homogeneous lithological compositions. These variances exhibit a striking alignment with fault lines and their associated tributaries by juxtaposing the underlying river profile with active structure, rock hardiness attributes, and associated geological features. This context lends itself to the identification of both lithological and tectonic knickpoints. Intriguingly, past investigations have failed to document landslide activity in this area. The residual *ksn* values exhibit a robust correlation with rock erodibility, primarily stemming from the juxtaposition of the Pütürge metamorphics and Maden Melange rocks.

Formed by the left-lateral strike-slip Pütürge segment, the Şiro Valley lies at the center of a debate regarding the nature of the fault. The left-lateral strike-slip nature of the Pütürge segment is supported by Emre et al. (2018) and Duman and Emre (2013), while Çetin et al. (2003) argue that it exhibits a more complex scenario, including both left-lateral strike-slip behavior and normal fault characteristics, particularly along the NE-SW-directed Şiro Valley. Despite the ongoing debate regarding the exact classification of the Pütürge segment, geological and geomorphological evidence confirms its role as an active tectonic boundary for the Şiro Valley, in agreement with Khalifa et al. (2018).

The valley is bordered by active strike-slip faults dipping to the southeast and northwest, with a significant normal fault component. This characterization is supported by morphometric analysis of ten large to moderate drainage basins controlled by the fault system.

Noticeably, the Şiro Valley is constrained by southeast- and northwest-dipping active strike-slip faults, predominantly demonstrating a normal fault component. This characterization is supported by morphometric analyses of ten large to moderate drainage basins controlled by the fault system. In this comprehensive analysis, a variety of morphometric indices, such as *Smf*, *Vf*, *AF*, *HI*, *HC*, *Bs*, and *ksn*, were employed to evaluate the drainage areas impacted by the Pütürge segment. Furthermore, this analysis additionally incorporated the Iat index, which combined the results from the individual geomorphic indices. This combined index provides a more comprehensive understanding of the spatial distribution of relative tectonic activity across the drainage basins affected by the Pütürge segment.

Uplift rates are commonly estimated, and relative tectonic activity is assessed using Smf and Vf. By analyzing *Smf* values from mountain fronts adjacent to the Pütürge segment and *Vf* values from its drainage areas, the fault activity and uplift rates can be inferred. These morphometric analyses, particularly those of *Smf* and *Vf*, become more instrumental in estimating long-term slip rates and understanding relative uplift rates through regression analyses, as proposed by Rockwell et al. (1984). *Smf*, which serves as a dual indicator of erosion and tectonic activity, reveals diverse linear patterns of mountain fronts across various elevation gradients within a specified region (Rockwell et al., 1984; Koukouvelas et al., 2018). This dynamic interplay, driven by both erosional processes and tectonic forces, often results in mountain fronts exhibiting broader and more sinuous curvatures (Bull and McFadden, 1977).

The *Smf* values we obtained indicate a significant level of tectonic activity across all mountain fronts. Remarkably, the S1 and S3 segments show the lowest *Smf* values, in contrast to the highest values recorded in the S2 and S4 segments (Fig. 10). Consequently, the relatively subdued tectonic activity suggested by the *Smf* values in the S1 and S3 segments corresponds to mountain fronts with flatter profiles than those in other regions.

Vf serves as a pivotal geomorphic index for delineating the dominance of tectonic or erosional processes within a basin. Low *Vf* values highlight heightened tectonic activity, fostering the formation of V-shaped valleys, while high *Vf* values indicate the prevalence of fluvial or bed-level erosional processes, resulting in U-shaped valleys (Bull and

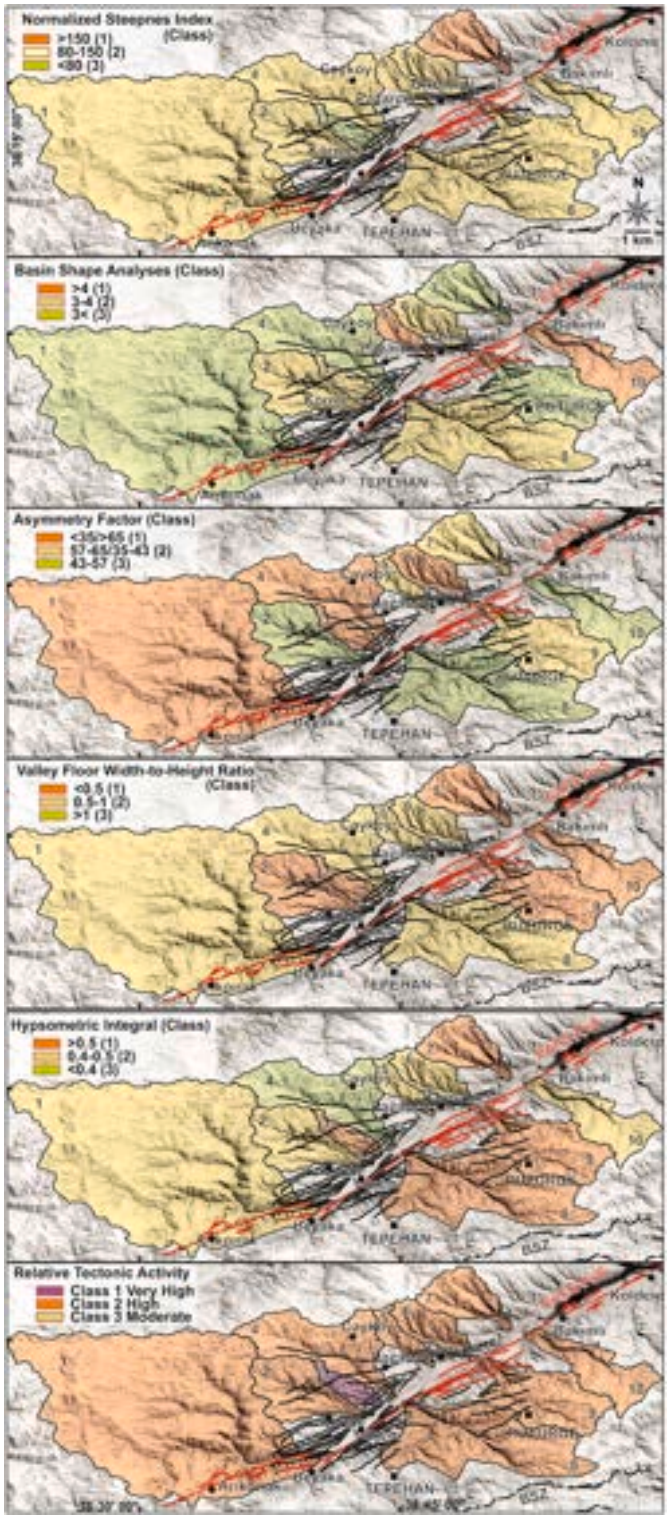

Fig. 10. Distribution of relative tectonic activity and geomorphic index classes in drainage basins in the Şiro Valley (The dark area in the upper-right corner represents the course of the Fırat River).

McFadden, 1977). In particular, drainage basins 2, 3, 7, 9, and 10 exhibit the lowest *Vf* values, indicative of V-shaped valleys, while drainage basins 1, 4, 5, 6, and 8 display elevated values, reflecting U-shaped valleys attributed to dominant erosional regimes during tectonic activity (Table 3, Fig. 10).

The combination of morphological traits that signal a linear mountain front, coupled with low *Smf* and *Vf* values and supported by seismic data (Londono et al., 2020), collectively underscores the active nature of the Pütürge segment, which is characterized by oblique transtensional kinematics. Our analysis reveals ostensibly subdued *Smf* and *Vf* values, indicating that this segment is an active mountain front with an inferred empirical uplift rate exceeding 0.5 mm/yr (Fig. 10). Intriguingly, high *ksn* values, along with knickpoints and stream deflections, further fortify the evidence of Quaternary activity along the Pütürge segment of the EAFS. Morphometric uplift rates in transtensional tectonic regimes often display significant spatial variability. Regions primarily influenced by extensional forces tend to experience lower uplift rates or subsidence, whereas areas affected by block rotation, fault interaction, or localized compression frequently exhibit higher uplift rates. These rates, inferred from geomorphic indices such as river terraces or fault scarp heights, provide critical insights into regions where vertical movements are most pronounced within transtensional tectonic settings (Burbank and Anderson, 2011). The transtensional tectonic regime dominating the Şiro Valley, characterized by a significant normal fault component combined with strike-slip motion, drives both the valley's subsidence and its geomorphic development. Furthermore, the fault geometry and oblique characteristics of the Pütürge segment and block rotations along the East Anatolian Fault System (EAFS) contribute to the increased uplift rates observed in this region.

In drainage basin analyses, symmetrical characteristics along the main river flanks are typically assumed. However, regional-scale factors, including resistant rock unit collapse, tectonic tilting, or fault zones (acting independently or in combination), can induce lateral river migration, resulting in asymmetric drainage areas on opposite sides of the main channel. Utilizing the *AF* indices to assess the lateral migration of the main river enables the determination of the tilt direction within the drainage area. The results indicate a marked asymmetric pattern in 70% of the drainage basins, while the remaining 30% exhibit a symmetric pattern (Table 3). This evidence underscores that a significant portion (70%) of the drainage basins have experienced surface tilting, primarily directed eastward in the vicinity of the Şiro Valley, controlled by the Pütürge segment (Fig. 10).

The *HI-HC* index is a crucial morphometric tool that offers insights into relatively active tectonic movements and dynamic erosion factors influenced by various elements, including climatic conditions, rock strength, erosion dynamics, and active fault activity (El Hamdouni et al., 2008; Softa, 2022). Analysis of the estimated *HI* values across basins 1 to 10 reveals a range of basin developmental stages. Higher *HI* values indicate youthful and mature basins, except for basin 3. Conversely, lower *HI* values suggest more advanced stages of basin evolution, particularly in the eastern extent of the fault-controlled basin. Flat-S-shaped or mature basins are partly attributed to rejuvenation processes facilitated by fault connections within the Pütürge segment. Additionally, many basins exhibit elongated or semi-elongated morphologies. Consistent with the classification by Ellias (2015), drainage basins 1, 4, 7, and 9 are categorized into class 3, indicating rapid uplift processes (Fig. 10).

The short-term evolution of landscapes relies on geomorphological insights derived from drainage basins, facilitating a more profound understanding of erosion dynamics and the ongoing interplay between rock uplift and climatic factors (Keller and Pinter, 2002). Given the uniform geology and minimal climatic variability within the Şiro Valley and its vicinity, the identification of multiple knickpoints accompanied by increased *ksn* values along the analyzed drainage basins offers compelling evidence of ongoing incision and erosion processes. This activity is potentially attributable to ongoing tectonic activity in the study area. Mainly, the occurrence of stream knickpoints and increased *ksn* values predominantly situated northwest of the Şiro Valley, where notable tectonic landforms are more prevalent (Fig. 10), suggests the presence of Quaternary active faults and a concurrent phase of active incision upstream. The *ksn* index has emerged as an exceptionally responsive tool for capturing variations in erosion rates, thereby furnishing crucial insights into regional uplift patterns (Ouimet et al.,

2009; Kirby and Whipple, 2012).

The distribution of knickpoints across a topography is valuable for deciphering regional strike-slip tectonics with a normal component. For example, progressive variations in rock uplift rates should manifest as knickpoints distributed evenly along uniform contour lines, assuming a consistent vertical propagation rate dictated by stream erosion dynamics (Whipple and Tucker, 1999; Wobus et al., 2006; Whipple et al., 2013). Conversely, sudden shifts in rock uplift rates typically appear as straight patterns, often aligning with structural trends, and are indicative of detached strike-slip tectonics linked to normal faulting processes (Whipple et al., 2013). The prevalence of elevated *ksn* values following the NE−SW striking Pütürge segment within the broader region is noticeable even to the bare eyes; however, some deviation in *ksn* values near the drainage divide suggests differentiated activity within the segment. Geochronological data from the literature on the river terraces affected by the Pütürge segment (Çetin et al., 2003) signified rapid exhumation during the Pleistocene epoch. This remark indicates that sustained fault activation extended back at least 11,000 years, followed by a phase of tectonic quiescence and subsequent uplift events since the Quaternary, culminating in northwesterly migration under the influence of the NE-SW-striking Pütürge segment.

Furthermore, all morphometric indices were collectively assessed following the criteria outlined by El Hamdouni et al. (2008) to delineate classes of relative tectonic activity. The classification included four categories: very high ($1.0 < Iat < 1.5$), high ($1.5 < Iat < 2$), moderate ($2.0 < Iat < 2.5$), and low ($Iat > 2.5$). Our analysis revealed a concentration of high tectonic activity along the entirety of the Pütürge segment, predominantly characterized by its normal fault component. However, while drainage basins in the northern valley exhibit rather high tectonic activity, the southern periphery of this valley demonstrates high tectonic activity (Fig. 10). This disparity stems from differential uplift mechanisms, possibly influenced by the greater activity of the strike-slip fault in the northern branch of the Şiro Valley compared to its southern counterpart, as Topal and Softa (2023) suggested.

Our analysis of divide stability reveals variations in how drainage divides have moved over time. In dynamic landscapes, the incessant migration of watershed divides stems from the geometric interplay among neighboring basins featuring diverse erosion rates and altitudes (Goren et al., 2014). The variations in relief and gradient observed in segments D1 and D2 (see Fig. 5), particularly the high *ksn* values and increased uplift rates, suggest that these divides are undergoing active southwestward migration. Numerical simulations by Whipple et al. (2017) show that river profiles rapidly adjust to tectonic disturbances before drainage migration begins. In that sense, we propose that anomalies in relief and gradients in segments D1-2 (see Fig. 5) represent an early stage of southwestward divide migration.

While the χ values along the basins in the Pütürge segment show profiles ranging from straight to smoothly convex (e.g., Basins 1, 2, 4), these deviations from the expected linear trend indicate a recent disruption (Perron and Royden, 2013; Willett et al., 2014). Nonetheless, this disruption has not yet substantially impacted the stability of the divide or the sizes of the drainage basins on either side (see Fig. 5). Therefore, divide analysis for segments D3 and D4, using Gilbert metrics and χ, suggests a stable divide under transient, quasi-steady-state conditions.

5.3. Slip rate interpretation of the Pütürge segment along the Şiro Valley

Early estimates of the slip rate along the EAFS vary according to the data collection and analysis method. Overall, geological observations suggest a slip rate between 4 mm and 13.5 mm/year (Arpat and Şaroğlu, 1972; Seymen and Aydın, 1972; Yürür and Chorowicz, 1998; Koçyiğit et al., 2001; Aksoy et al., 2007; Herece, 2008). Kinematic analysis models, which provide a different approach but are compatible with slip rates, indicate rates ranging from 7.8 mm to 19 mm per year (Lyberis et al., 1992; Westaway, 2004, 2006). Cavalié and Jonsson (2014) proposed a slip rate of approximately 13 mm per year using interferometric synthetic aperture radar (InSAR) technology. However, as Kurt et al. (2023) emphasized, it becomes challenging for InSAR to represent the actual values in areas experiencing ongoing creep precisely. In addition, GPS measurements, another crucial and up-to-date data source, show slip rates of 4 mm–15 mm/year along the EAFS, while each study provides figures in this broad slip rate array (Oral et al., 1992; Barka and Reilinger, 1997; McClusky et al., 2000; Westaway, 2003; Reilinger et al., 2006; Özener et al., 2010; Aktuğ et al., 2016). Walters et al. (2014) compared the slip rates inferred from InSAR and GPS data and demonstrated that while slip rates can be calculated from InSAR data alone without GPS data, certain crucial factors (e.g., crustal rotation) can lead to erroneous results. Finally, seismological analysis provides a broader range of estimated slip rates than previous methods, varying from 6 mm to 31 mm/year (Taymaz et al., 1991; Kiratzi, 1993).

Along with slip movement, the locking depth is used to evaluate slip rates up to the state where creeping is active. The locking depth refers to the depth within the crust where tectonic plates are thought to be effectively locked together due to apparent friction along a fault line, thereby preventing movement. This depth represents the depth below which the strain accumulates along the fault due to the movement of tectonic plates, potentially leading to earthquakes when the accumulated strain is released. Among various findings, Walters et al. (2014) presented two crucial remarks for understanding the EAFS, particularly the Pütürge Segment. One finding indicates that the average locking depth for a large region covering the Pütürge segment is approximately 25 km, slightly more significant than the earthquake hypocentral depth but not abnormal for an area with active seismicity that mainly produces shallow and moderate earthquakes. However, this figure is generally slightly more significant than the average locking depth for the EAFS, as in the same study.

Similarly, as ongoing movement persists in the region, this phenomenon signifies that stress accumulates along the fault and is active. If this stress is released through an earthquake, it can lead to significant seismic activity depending on various factors, such as the magnitude of the earthquake and the depth of the epicenter. The second observation of Walters et al. (2014) emphasized segmented behavior, contradicting the early belief that the EAFS behaves as a block-like structure. Çakır et al. (2023) examined slips in the aftermath of the January 2020 Mw 6.8 Elazığ earthquake and offered some critical insight into both the progression of regional seismicity and the concept of creeping faults in a general sense. They noted that the areas of strike-slip faults where movement is gradual might halt or weaken earthquake activity, commonly ascribed to their limited potential for slip or to the frictional properties of the faulting planes, making movement less likely with increased friction. An overarching remark drawn from the observations made by Çakır et al. (2023) is that the spatial alignment of slip distributions across different time periods indicates a dynamic compensation mechanism within fault systems.

By recompiling and analyzing data from the two most well-known studies based on GPS data, namely, Reilinger et al. (2006) and the more up-to-date Kurt et al. (2023), we present the distributions of annual ground velocities specific to the study area and its vicinity in Figs. 11 and 12. Fig. 11 an illustrates that the examined drainage basins are experiencing steady motion, while Fig. 11b reveals two distinct movement characteristics within the Şiro Valley. The northern basins exhibit motion with a velocity of 18 mm/year, whereas the southern basins and some portions of the northern basins are moving at a slightly slower pace, approximately 1 mm/year less than their northern counterparts. Interestingly, the delineation of movement begins from the new fault traces identified during our fieldwork. Additionally, our analysis indicates that the northern basins are more active than the southern ones according to morphometric indices, which aligns with the overall portrayal in Fig. 11b. Fig. 11c depicts the time-weighted deformation over the period between 2006 and 2024, derived from two models, while Fig. 11d displays the average deformation values from the two

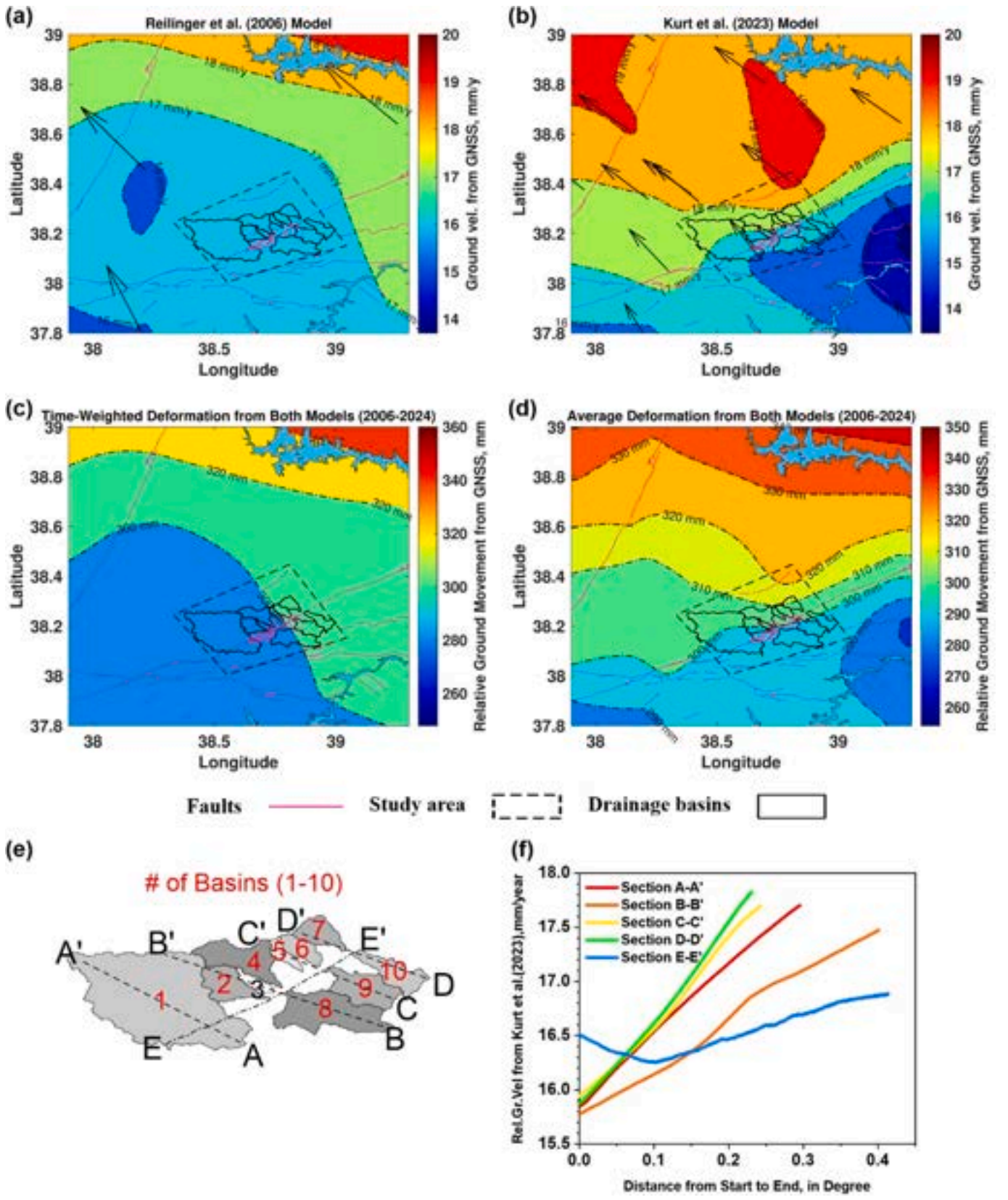

Fig. 11. a) Ground velocity distribution from Reilinger et al. (2006). b) Ground velocity distribution from Kurt et al. (2023). c) Time-weighted average deformation values from the two velocity models over the time span (2006–2024). d) Average deformation values from the two velocity models over time (2006–2024). e) Examined basins and cross-sections. f) Deformation profiles along the cross-sections drawn on the basins.

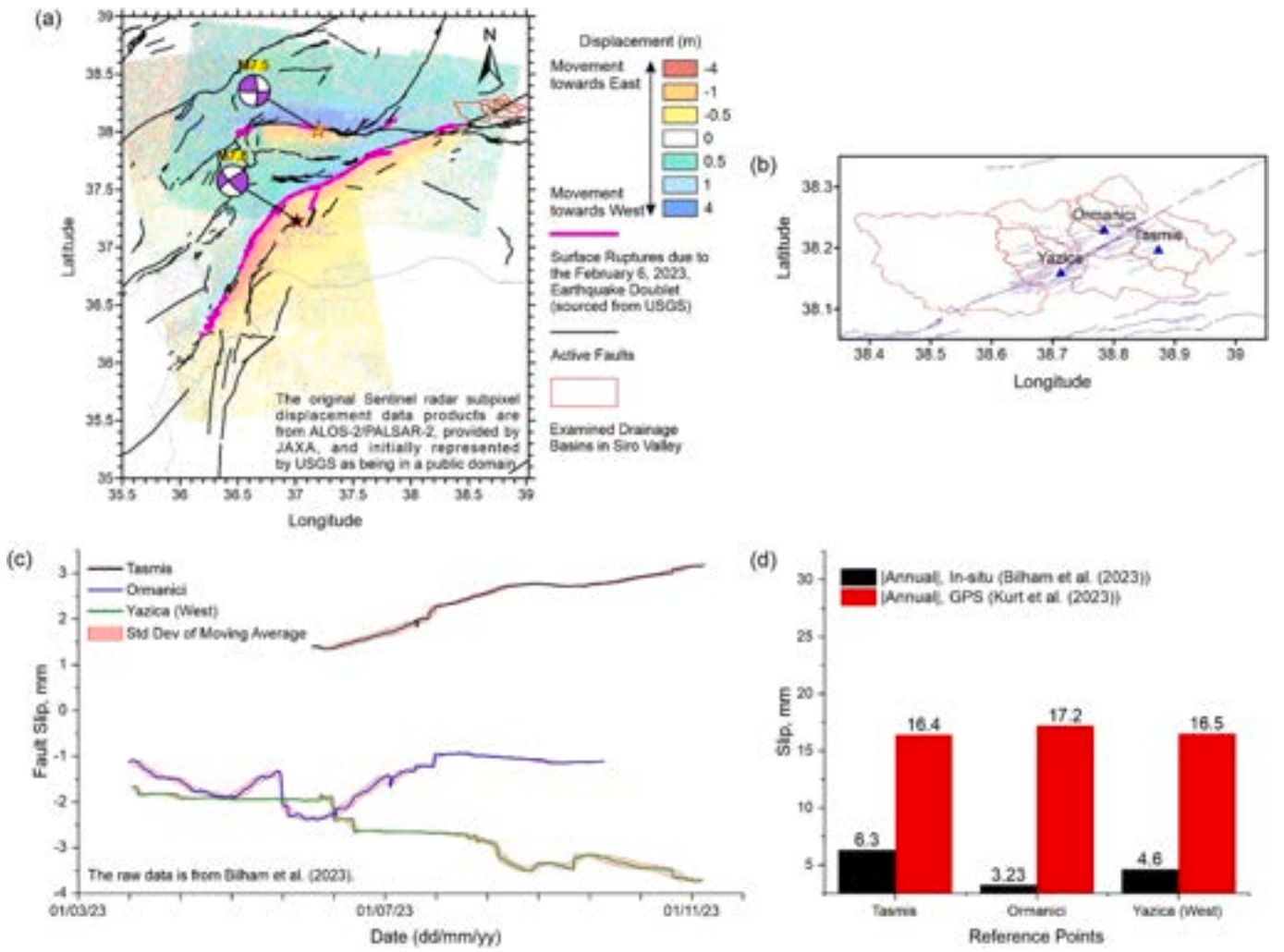

Fig. 12. a) Coseismic displacement during the February 6, 2023 earthquake doublet, b) Location map of the examined basins of the Şiro Valley and reference points for slip comparison, c) slip measurements against elapsed time at the reference locations after the doublet, d) difference between the annual infield deformations and GPS-based velocity measurements.

velocity models over the same time span.

In the time-weighted computation, the model proposed by Reilinger et al. (2006) takes precedence, significantly influencing the deformation pattern. Conversely, the values from Kurt et al. (2023) introduce alterations to this pattern. However, when averaging the values from both models, the resulting deformation pattern aligns more closely with the original model by Kurt et al. (2023). Fig. 11c delineates two deformed zones, roughly east and west, while Fig. 11d further defines two deformation zones oriented north and south. The observations from Fig. 11c corroborate our previous findings regarding the movement of the basins. Nevertheless, over the 18-year deformation period, there is a notable difference in total deformation between basins in the two different zones, amounting to 10 mm. This figure indicates that the basins are experiencing relative motion within themselves at a 0.55 mm/year velocity.

Fig. 11e displays all the basins examined and cross-sections drawn, while Fig. 11f illustrates the deformation profiles along the cross-sections outlined in Fig. 11e. Notably, the valley bottom and the main fault line track exhibit nonlinear motion, with the eastern tip of the valley experiencing the highest velocity, consistent with the observations in Fig. 11c and the abovementioned observations. Sections D-D and C-C demonstrate the most rapid separation, followed by section A-A. Our field observations and morphological analysis revealed that basins 1 and 4 exhibit faster movement than the other basins. Additionally, it is evident from this analysis that basin ten is developing at a slower pace than basin 7.

It is evident from the instrumental seismic record that the EAFS experiences relatively fewer large, catastrophic earthquakes than the North Anatolian Fault Zone (NAFZ). However, the EAFS has a history of significant seismic activity predating the instrumental era, as Pousse-Beltran et al. (2020) summarized. This seismic quiescence changed after the January 2020, 24, Mw: 6.8 Sivrice (Elazığ) earthquake, which occurred on the Sivrice-Pütürge segment. Konca et al. (2021) developed a kinematic faulting model using strong ground motions, GNSS, teleseismic waveforms, and InSAR data, revealing a rupture of approximately 45 km along the Sivrice-Pütürge segment. Additionally, Tatar et al. (2020) conducted large-scale field investigations and computational models and revealed that while early expected or postulated long-range surface faulting was not observed, some short-range surface deformations were detected.

For a considerable time, the absence of surface rupture following the recorded Mw: 6.8 earthquake along the Pütürge fault puzzled researchers and led to numerous attempts at explanation. Despite the magnitude of the earthquake, Pousse-Beltran et al. (2020) demonstrated and justified a significant lack of slip along the Pütürge fault at shallow depths. This deficiency in slip implied that the earthquake did not fully release all the accumulated stress or that the stress release occurred further from the fault surface than expected. Furthermore, the gradual

fault movement after the main seismic event was insufficient to compensate for this deficit. Essentially, even after the mainshock and subsequent minor adjustments in the fault (afterslip), there remains an unaddressed gap in stress release at shallow depths, which could impact the seismic behavior of the fault in the future. Tatar et al. (2020) explored the same challenge and linked the absence of anticipated surface ruptures along the Pütürge segment post-2020 earthquake to various factors, including the limited extent of left-lateral strike-slip movement to the surface, the left-lateral rotational motion of the fault around a vertical axis during the quake, the restraining bend nature of the Pütürge segment, and the dominant influence of the Pütürge metamorphic rocks along the fault line.

On the one hand, in simpler terms, subshear rupture refers to a motion whose speed is slower than the speed at which shear waves propagate through the crust. On the other hand, supershear rupture is expected to occur when the speed of the rupture motion far exceeds the shear wave speed of the material surrounding the fault plane. All the shear in the 2020 earthquake fell into the subshear category. According to Ren et al. (2023), the 2023 doublet earthquake on the EAFS generated shear cycles that propagated in two directions during each significant earthquake. Ren et al. (2023) argued that during the M7.5 earthquake, the second of the doublet, the two-pronged rupture exhibited apparent sub- and supershear movements, initiating motion in the Pazarcik segment, with its main effects being buffered in front of the Pütürge segment. Barbot et al. (2023) interpreted this behavior as the rupture halting its southward movement where the EAFS ends while diminishing northward into the Pütürge segment, indicating a seismic gap with significant seismic risk associated with as yet underdeveloped faulting systems.

Recent analyses of seismic events, including the Sivrice earthquake and the 2023 doublet, massively underscore the complex conundrum of the seismotectonics and structural dynamics of the East Anatolian Fault system. The unusual and unexpected slip amounts evidenced in the 2023 events indicate that they could belong to a larger supercycle pattern, suggesting significant underlying fault complexity (Billi et al., 2024). The Mw 7.8 earthquake's rupture involved at least three primary segments and was initiated along uncharted fault lines, revealing previously undiscovered intricacies within the EAF system (Magen et al., 2024). Notably, the Mw 7.6 aftershock generated more significant surface offsets (8.5 m) than the mainshock, showcasing more complex stress interactions across the fault segments than previously thought (Magen et al., 2024). It was noted that the differences in seismic slip distribution and stress release among various segments highlight the tectonic heterogeneity of the all-out system (Chen et al., 2024). More so, historical seismic patterns revealed an apparent southwestward migration of earthquake clusters, implying a mechanistically systematized stress transfer throughout the complete fault system (Karabulut et al., 2022; Billi et al., 2024). Having all these remarks taped, these findings directly manifest that the Pütürge segment functions within an intricately interconnected fault network, where stress transfer and rupture dynamics are more complex than previously understood, highlighting the need for more detailed seismic hazard assessments in the area.In that sense, we compiled various datasets and generated a composite figure to illustrate the extent of coseismic and postseismic movement along the Pütürge fault. In Fig. 12a, the Earth's deformation and direction of movement resulting from the doublet earthquake are depicted in color. The basin zones of the Şiro Valley investigated in our study are situated just beyond where the westernmost deformation ends. Upon examining the moving fault segments, deformed fault lines are observed at the onset of the western tip of the main fault trunk dividing the valley. This remark suggests that despite massive slip amounts and stress drops observed in the EAF system, the Pütürge segment remained locked during the doublet earthquakes. Additionally, despite extensive fieldwork, we did not observe a tractable prolonged valley-through fault yielded due to the doublets. This observation prompts a burning question about the behavior of the Pütürge fault before and after the doublet and whether or not changes in slip behavior indicate any anomalies or evolutionary traits.

Using data on the distribution, direction, and magnitude of ground motion during February 2023, 6 earthquakes provided by the USGS, and fault fractures identified through remote sensing by the USGS, we overlaid Türkiye's active fault map and the basin boundaries of this study to create Fig. 12a. According to the figure, movement ceased at the triple junction located at the western end of the Şiro Valley basin. This behavior corresponds with the intricate fault segmentation patterns documented in the 2023 doublet, where rupture propagation exhibited distinct characteristics unique to each segment (Magen et al., 2024). Deformation was notably limited, particularly in the vicinity of basins close to the area through which the M7.5 earthquake was expected to prolong its primary impact. This limited deformation is especially noteworthy considering the unexampled surface offsets reaching up to 8.5 m reportedly observed in other areas during the Mw 7.6 event (Magen et al., 2024). This resulted in a relatively east-west separation along the fault line running through the middle of the basins. The fault rupture did not extend into the Şiro Valley and remained locked at the triple junction near the valley's entrance. This locking behavior could be associated with the varying degrees of seismic slip concentration observed across different segments of the EAFS (Billi et al., 2024). Fig. 12b illustrates only three locations where creepmeters were installed along the EAFS by Prof. Roger Bilham. In Fig. 12c, we reprocessed the creep data given in Bilham et al. (2023), spanning roughly nine months. Additionally, Özarpacı et al. (2024) provide further evidence supporting aseismic deformation along the unruptured portion of the Pütürge segment following the 2020 Sivrice-Doğanyol earthquake and the 2023 Kahramanmaraş earthquake doublet. This pattern of aseismic deformation aligns with the broader supercycle behavior identified along the East Anatolian Fault (Billi et al., 2024). Although these creep data do not provide an annual overview, we extrapolated them to obtain year-long averaged data and compared them with the annual slip rate data from Kurt et al. (2023) in Fig. 12d. Upon examining all panels together, it becomes evident that the Pütürge fault is currently in a slip accumulation phase. The accumulation phase that has not yet been enlightened to date is rather substantial in light of the documented and thenceforwardly more focused southwestward migration of seismic activity along the EAF (Billi et al., 2024; Karabulut et al., 2022). However, this does not necessarily mean that it was not in a slip accumulation phase before the doublet earthquake or vice versa. Nevertheless, the slips fall outside the range reported by Kurt et al. (2023) and Reilinger et al. (2006), betokening possible modifications to the stress regime right subsequent to the events of 2023, as recently demonstrated by the intricate stress drop patterns noted in the area (Chen et al., 2024).

We reiterate that this fault did not produce a surface rupture after the 2020 earthquake, and it was positioned in front of the supershear following the Mw: 7.8 earthquake of the 2023 doublet. This behavior remains remarkably consistent with the spatial and kinematic channeling patterns observed through the fault surface of the main trunk, as corroborated in a recent study (Billi et al., 2024). All these observations lead us to suggest that while creep activity is ongoing, the Pütürge segment is in a phase of slip accumulation, where it accumulates or redirects gradual stress or forms a wedge-like structure uplifting the Şiro Valley to the southwest. This collection phase comes to the fore and becomes particularly significant given the recent discovery of earthquake supercycle occurrences along the EAFS, where seismic ruptures exhibited a gradual southwestward migration pattern (Billi et al., 2024). In essence, all available information suggests a paradox: the Pütürge segment was in an interseismic locking phase from 2020 to 2023, and it continues to be in a locking phase from 2023 onward, indicating that certain portions of the fault remained locked during the period between at least two significant earthquakes, and it remains in the same position. This persistent locking behavior may be linked to the complex stress distribution patterns observed in the region, where varying stress drops

and fault heterogeneity (Chen et al., 2024; Magen et al., 2024) play crucial roles in the seismogenesis of the system.

6. Conclusion

This study aimed to investigate the least studied segment of the East Anatolian Fault System, called the Pütürge segment in southeast Türkiye, particularly focusing on the Şiro Valley, to better understand the comprehensive distribution of deformation in this area. The following conclusions can be drawn from this study.

1. The collective assessment of morphometric indices, including the Smf, Vf, HI-HC index, ksn and χ values, and deformation pattern analyses, provided a comprehensive understanding of the neotectonic activity along the Pütürge segment. In particular, morphometric analysis revealed distinctive characteristics consistent with active tectonic deformation, such as steep mountain fronts, asymmetric drainage patterns, and rapid erosion rates. These features indicate ongoing crustal movements and faulting, which are typical manifestations of tectonic activity along normal fault segments.
2. The Iat analysis can be linked to the broader kinematic behavior of the fault system in the region. The eastward-directed tilting observed in the drainage basins corresponds to the expected displacement patterns associated with the oblique transtensional kinematics of the Pütürge segment. As the fault accommodates both strike-slip and extensional movements, it can induce tilting of the surrounding landscape, leading to asymmetric drainage basin patterns. Furthermore, this observation reinforces the preconceived notion that the Pütürge segment plays a significant role in controlling all-out regional geomorphic evolution. The eastward tilting of drainage basins implies ongoing tectonic activity along the fault, contributing to landscape deformation and shaping drainage networks over geological timescales.
3. The Şiro Valley is deformed by the Pütürge segment under the influence of the extensional regime accompanying the dominant strike-slip tectonic regime, with a compressional stress state approximately NE–SW trending and an extensional stress state approximately NW–SE trending.
4. The comparison of slip rates by Bilham et al. (2023) and velocity models by Reilinger et al. (2006) and Kurt et al. (2023) provided valuable insights into the dynamic behavior of faults, particularly in regions where faults are creeping or in a collection phase. We reprocessed the data, compared them with our findings, and showed that variations in ground velocities and strain accumulation along fault segments are apparent, suggesting that the fault behaves at a slower rate than previously observed. This slower behavior implies that the fault is potentially accumulating energy over time, increasing the risk of future seismic events.

The findings of this study pave the way for further research into the dynamics of the Pütürge segment and other yet unresolved active segments. Even the historical seismicity record underscores the pivotal role of the Pütürge segment in the seismotectonic evolution and dynamics of the EAFS. A much deeper understanding of the Pütürge Segment is essential to better assess and mitigate its seismic risks, ensuring more effective preparedness and response strategies, thereby underscoring the urgent need for enhanced surveillance and more detailed studies.

Data sources, availability, and software tools employed

In addition to the infield data collected from the study area, several external data sources and software tools were utilized to support the analyses. Integrating diverse tools and datasets facilitated a comprehensive analysis, ensuring robust results and refined conclusions within this study.

The focal mechanism of the earthquakes ($M_W \geq 3.0$) was sourced from the Disaster and Emergency Management Presidency of Türkiye (available at https://deprem.afad.gov.tr/event-focal-mechanism). We employed simplified geological maps at a scale of 1:100,000, sourced from the Geological Maps of Türkiye (available at https://www.mta.gov.tr/en/maps). These maps were georectified, georeferenced, and digitized using several GIS software packages.

Various software tools were used in our research to enhance the processing and analysis capabilities. MATLAB® R2023b, provided under an academic license by Karadeniz Technical University (available at https://www.mathworks.com/products/matlab.html), was instrumental in generating some figures and maps presented in this article. Similarly, ArcGIS® software, which is also licensed through Karadeniz Technical University and Fırat University (available at https://www.esri.com/en-us/arcgis/about-arcgis/overview), and QGIS (version 3.34 LTR) (available at https://qgis.org/tr/site/forusers/download.html) were utilized for various analyses and map productions. A MATLAB® utility called TopoToolbox version 2 (Schwanghart and Kuhn, 2010; Schwanghart and Scherler, 2014) (available at https://topotoolbox.wordpress.com/download/) was used for the digital elevation model-based analyses. Additionally, the MATLAB® tool WinTensor 5.9.1 (Delvaux and Sperner, 2003) (available at https://damiendelvaux.be/Tensor/WinTensor/win-tensor_download.html) was used for the fault kinematic analyses and tectonic stress tensor inversions.

All data initially obtained within the scope of this study are detailed in this article. For those interested in further analysis, the data can be made available upon reasonable request to the corresponding author.

CRediT authorship contribution statement

Elif Akgün: Writing – review & editing, Supervision, Project administration, Investigation, Formal analysis, Data curation, Conceptualization. **Savaş Topal:** Writing – original draft, Software, Methodology, Investigation, Formal analysis. **Mustafa Softa:** Writing – review & editing, Methodology, Investigation, Formal analysis, Data curation. **Murat Nas:** Writing – review & editing, Software, Methodology, Investigation, Data curation. **Serkan Gürgöze:** Writing – original draft, Software, Methodology, Investigation, Data curation. **Hasan Sözbilir:** Writing – review & editing, Investigation, Formal analysis, Data curation. **Ercan Aksoy:** Writing – original draft, Investigation, Formal analysis, Data curation. **Joel Q.G. Spencer:** Writing – review & editing, Investigation, Data curation. **Mehmet Yüksel:** Writing – original draft, Methodology, Data curation.

Funding information

This study was supported by the Scientific and Technological Research Council of Türkiye (TUBITAK) under Grant Number 122Y266. The authors thank TUBITAK for their support.

Declaration of competing interest

The authors declare that they have no known competing financial interests or personal relationships that could have appeared to influence the work reported in this paper.

Acknowledgments

This study is dedicated to Özge Koçbulut, who was taken from us too soon, and to her father, Fikret Koçbulut, whose unwavering support has always been with us. This research was supported by the Turkish government through the 3501 Project under the Advanced Carrier Support Program managed by TÜBİTAK. We extend our sincere gratitude to R. Bilham for sharing his creepmeter raw data and providing a thorough review concerning fault creep. Additionally, we express our sincere appreciation to the staff at the KADOIL petrol station and the residents of Pütürge for their hospitality, open-heartedness, and patience despite the

extreme temperatures reaching 50 °C. Furthermore, we would like to thank Malatya University-Mehmet Şahin Nalbant guest house for providing accommodations. Lastly, we sincerely acknowledge the anonymous referees for their valuable criticisms and insightful feedback, which significantly contributed to the improvement of this manuscript.

Data availability

Data will be made available on request.

References

AFAD, 2023. Presidency of disaster and emergency management, ankara. Earthquake catalogue. https://deprem.afad.gov.tr/event-catalog. (Accessed 13 February 2023).
Akbaş, B., Akdeniz, N., et al., 2011. 1:1.250.000 Ölçekli Türkiye Jeoloji Haritası. Maden Tetkik Ve Arama Genel Müdürlüğü Yayını, Ankara-Türkiye. http://yerbilimleri.mta.gov.tr/.
Akgün, E., 2021. Determination of recent stress states from the Sivrice-Doğanyol earthquake and the post-seismic activities. In: 2nd International Mathematic, Architecture and Engineering Conference (IMAEC).
Akgün, E., İnceöz, M., 2021. Tectonic evaluation of the central part of the East Anatolian Fault Zone, eastern Turkey. Turk. J. Earth Sci. 30 (7), 928–947.
Aksoy, E., İnceöz, M., Koçyiğit, A., 2007. Lake hazar basin: a negative flower structure on the East Anatolian Fault System (EAFS), se Turkey. Turk. J. Earth Sci. 16, 319–338.
Aksoy, E., Akgün, E., Softa, M., Koçbulut, F., Sözbilir, H., Tatar, O., Çolak Erol, S., 2023. 6 şubat 2023 Pazarcık (Kahramanmaraş) depreminin doğu anadolu fay zonu Erkenek ve Pazarcık segmentleri üzerindeki etkisi: çelikhan-gölbaşı (adıyaman) arasından gözlemler. Türk Deprem Araştırma Dergisi 5 (1), 85–104.
Aktuğ, B., Özener, H., Doğru, A., Sabuncu, A., Turgut, B., Halıcıoğlu, K., Yılmaz, O., Havazlı, E., 2016. Slip rates and seismic potential on the East Anatolian Fault System using an improved GPS velocity field. J. Geodyn. 94, 1–12.
Alipoor, R., Poorkermani, M., Zare, M., El Hamdouni, R., 2011. Active tectonic assessment around Rudbar Lorestan damsite, high Zagros belt (SW of Iran). Geomorphology 128 (1–2), 1–14.
Ambraseys, N.N., 1989. Temporary seismic, quiescence: SE Turkey. Geophys. J. Int. 96, 311–331.
Ambraseys, N.N., Finkel, C., 1995. The Seismicity of Türkiye Earthquake of 19 December 1977 and the Seismicity of the Adjacent Areas 1500-1800. Eren Yayıncılık ve Kitapçılık, p. 240.
Ambraseys, N.N., Jackson, J.A., 1998. Faulting associated with historical and recent earthquakes in the Eastern Mediterranean region. Geophys. J. Int. 133, 390.
Anderson, E.M., 1951. The Dynamics of Faulting and Dike Formation with Application to Britain, second ed. Oliver and Boyd, Edinburgh, p. 206.
Angelier, J., 1990. Inversion of field data in fault tectonics to obtain the regional stress III. A new rapid direct inversion method by analytical means. Geophys. J. Int. 103 (2), 363–376.
Angelier, J., 1994. Fault slip analysis and paleostress reconstruction. In: Hancock, P.L. (Ed.), Continental Deformation. Pergamon Press, Oxford, pp. 53–100.
Arger, J., Mitchell, J., Westaway, R., 2000. Neogene and Quaternary volcanism of south-eastern Turkey. In: Bozkurt, E., Winchester, J.A., Piper, J.D.A. (Eds.), Tectonics and Magmatism of Turkey and the Surrounding Area, vol. 173. Spec. Publ.-Geol. Soc. London, pp. 459–487.
Arpat, E., Şaroğlu, F., 1972. Doğu Anadolu Fayı ile ilgili bazı gözlem ve düşünceler. Bulletin of the Mineral Research and Exploration 73, 1–9.
Arpat, E., Şaroğlu, F., 1975. Türkiye'deki bazı önemli genç tektonik olaylar. Geol. Bull. Turk. 18 (1), 91–101.
Barbot, S., Luo, H., Wang, T., Hamiel, Y., Piatibratova, O., Javed, M.T., Braitenberg, C., Gurbuz, G., 2023. Slip distribution of the february 6, 2023 Mw 7.8 and Mw 7.6, Kahramanmaraş, Turkey earthquake sequence in the East Anatolian Fault Zone. Seismica 2 (3). https://doi.org/10.26443/seismica.v2i3.502.
Barka, A.A., Kadinsky-Cade, K., 1988. Strike-slip fault geometry and its influence on eartquake activity. Tectonics 7 (3), 663–684.
Barka, A.A., Reilinger, R., 1997. Active tectonics of the EasternMediterranean region: deduced from GPS, neotectonic and seis-micity data. Ann. Geophys.-Italy, XL.
Bilham, R., Ayruk, E.T., Turğut, M., İrgüren, R., Köküm, M., Elhisso, A., Farımaz, İ., Doğan, U., 2023. Afterslip and Triggered Slip Following the February 6 2023 Kahramanmaraş Earthquake Sequence, East Anatolian Fault, Türkiye. *3rd MedGU 2023 Annual Meeting*. Mediterranean Geosciences Union. Nov. 27-30, 2023 Istanbul.
Billi, A., Corbi, F., Cuffaro, M., et al., 2024. Seismic slip channeling along the East Anatolian Fault illuminates long-term supercycle behavior. Nat. Commun. 15, 8921. https://doi.org/10.1038/s41467-024-53234-0.
Bott, M.H.P., 1959. The mechanics of oblique slip faulting. Geol. Mag. 96, 109–117.
Bull, W.B., McFadden, L.D., 1977. Tectonic geomorphology north and south of the Garlock fault, California. In: Doehering, D.O. (Ed.), Geomorphology in Arid Regions, Proceedings of the *Eighth Annual Geomorphology Symposium*, pp. 115–138. Binghamton, New York.
Burbank, D.W., Anderson, R.S., 2011. Tectonic Geomorhology, second ed. Wiley Blackwell.
Çakır, Z., Doğan, U., Akoğlu, A.M., Ergintav, S., Özarpacı, S., Özdemir, A., Nozadkhalil, T., Çakır, N., Zabcı, C., Erkoç, M.H., Basmenji, M., Köküm, M., Bilham, R., 2023. Arrest of the Mw 6.8 January 24, 2020 Elaziğ (Turkey) earthquake by shallow fault creep. Earth Planet Sci. Lett. 608, 118085.
Cannon, P.J., 1976. Generation of explicit parameters for a quantitative geomorphic study of Mill Creek drainage basin. Oklahoma Geol. Notes 36 (1), 3–16.
Carey-Gailhardis, E., Mercier, J.L., 1987. A numerical method for determining the state of stress using focal mechanisms of earthquake populations: application to Tibetan teleseisms and microseismicity of Southern Peru. Earth Planet Sci. Lett. 82, 165–179.
Cavalié, O., Jonsson, S., 2014. Block-like plate movements in Eastern Anatolia observed by InSAR. Geophys. Res. Lett. 41 (1). https://doi.org/10.1002/2013GL058170.
Cederbom, C., Sinclair, H.D., Schlunegger, F., Rahn, M., 2004. Climate-induced rebound and exhumation of the European Alps. Geology 32 (8). https://doi.org/10.1130/G20491.1.
Çetin, H., Güneyli, H., 2002. Doğu anadolu fay sisteminin palu-hazar gölü ve hazar gölü-sincik segmentlerinin paleosismisitesi sonuç raporu. TÜBİTAK Proje No:197Y064.
Çetin, H., Güneyli, H., Mayer, L., 2003. Paleosismology of the palu-Lake Hazar segment of the East Anatolian Fault Zone, Turkey. Tectonophysics 374, 163–197.
Chen, X., Kwiatek, G., Bindi, D., Becker, D., Bohnhoff, M., Cotton, F., Martínez-Garzón, P., 2024. Stress drop variations of (A)seismic fault segments in the Sea of marmara region (northwestern Türkiye) supported by different methodological approaches. Bull. Seismol. Soc. Am. https://doi.org/10.1785/0120240128.
Dasgupta, S., Mukherjee, S., Vanik, N., Chatterjee, R., Pal, S.K., 2023. Paleostress analyses and rift kinematics of the petroliferous Barmer rift basin, western Rajasthan, India. Mar. Petrol. Geol. 156, 106442.
Delvaux, D., Sperner, B., 2003. New aspects of tectonic stress inversion with reference to the TENSOR program. Geological Society 212 (1), 75–100. London, Special Publications.
Delvaux, D., Moeys, R., Stapel, G., Petit, C., Levi, K., Miroshnichenko, A., Ruzhich, V., San'kov, V., 1997. Paleostress reconstructions and geodynamics of the Baikal region, Central Asia, Part 2. Cenozoic rifting. Tectonophysics 282, 1–38.
Dercourt, J., Zonenshain, L.P., Ricou, L.E., Kazmin, U.G., Le Pichon, X., et al., 1986. Geological evolution of the tethys belt from the atlantic to the pamirs since the lias. Tectonophysiscs 123, 241–315.
Dewey, J., Hempton, M.R., Kidd, W.S.F., Şaroğlu, F., Şengör, A.M.C., 1986. Shorteninig of continental lithosphere: the tectonics of Eastern Anatolia: a young collision zone. Collision Tectonics 19, 3–36.
Duman, T.Y., Emre, Ö., 2013. The East Anatolian Fault: Geometry, Segmentation and Jog Characteristics, vol. 372. Geological Society, London, Special Publications.
Duman, T.Y., Çan, T., Emre, Ö., Kadirioğlu, F.T., Başarır Baştürk, N., Kılıç, T., Arslan, S., Özalp, S., Kartal, R.F., Kalafat, D., Karakaya, F., Eroğlu Azak, T., Özel, N.M., Ergintav, S., Akkar, S., Altınok, Y., Tekin, S., Cingöz, A., Kurt, A.İ., 2018. Seismotectonics database of Turkey. Bull. Earthq. Eng. 16 (8), 3277–3316.
El Hamdouni, R., Irigaray, C., Fernández, T., Chacón, J., Keller, E.A., 2008. Assessment of relative active tectonics, southwest border of the Sierra Nevada (southern Spain). Geomorphology 96, 150–173.
Ellias, Z., 2015. The neotectonic activity along the lower khazir river by using SRTM image and geomorphic indices. Earth Sci. 1 (1), 50–58.
Emre, Ö., Duman, T.Y., Özalp, S., et al., 2018. Active fault database of Turkey. Bull. Earthq. Eng. 16 (8), 3229–3275.
Eyidoğan, E., 2021. Spatial and temporal analysis of seismicity of the Pütürge fault, and gutenberg-richter parameters before and after sivrice-doğanyol earthquake (Mw6.8) of january 24, 2020. Bulletin of the Earth Sciences Application and Research Centre of Hacettepe University 42 (3), 287–300.
Forte, A.M., Whipple, K.X., 2018. Criteria and tools for determining drainage divide stability. Earth Planet Sci. Lett. 493, 102–117. https://doi.org/10.1016/j.epsl.2018.04.026.
Gallen, S.F., Wegmann, K.W., 2017. River profile response to normal fault growth and linkage: an example from the Hellenic forearc of south-central Crete, Greece. Earth Surf. Dyn. 5, 161–186. https://doi.org/10.5194/esurf-5-161-2017.
Gilbert, G.K., 1987. Geology of the Henry Mountains. Government Printing Office, Washington, DC, USA.
Goren, L., Willett, S.D., Herman, F., Braun, J., 2014. Coupled numerical-analytical approach to landscape evolution modeling. Earth Surf. Process. Landforms 39, 522–545. https://doi.org/10.1002/esp.3514.
Gürboğa, Ş., Kayadibi, Ö., Akilli, H., Arikan, S., Tan, S., 2024. Preliminary results of the great Kahramanmaraş 6 february 2023 earthquakes (MW 7.7 and 7.6) and 20 february 2023 antakya earthquake (MW 6.4), eastern Türkiye. Turk. J. Earth Sci. 33 (1), 22–39.
Hack, J.T., 1957. Studies of Longitudinal Stream Profiles in Virginia and Maryland, vol. 294. US Government Printing Office.
Hare, P.W., Gardner, T.W., 1985. Geomorphic indicators of vertical neotectonism along converning plate margins, Nicoya Peninsula, Costa Rica. In: Morisawa, M., Hack, J.T. (Eds.), Tectonic Geomorphology (75-104), Proceedings of the 15th Annual Binghamton Geomorphology Symposium. Boston, MA: Allen&Unwin.
Harzali, M., Medhioub, E., Abdelmalak, M.M., Hamdouni, A., Troudi, H., 2023. Insights from the 06 february 2023 Mw 7.8 kahramanmaras earthquake evidence into an active strike-slip faulting along the East Anatolian Fault Zone. Acta Geodaetica et Geophysica 58 (15).
Hempton, M.R., 1987. Constraints on Arabian plate motion and extensional history of the Red Sea. Tectonics 6, 687–705.
Herece, E., 2008. Doğu Anadolu Fay (DAF) Atlası, vol. 13. Maden Tetkik ve Arama Genel Müdürlüğü, Special Publication Series.
Herece, E., Akay, E., 1992. Karlıova-çelikhan arasında doğu anadolu fayı. In: Proceeding of the 9th Petroleum Congress of Turkey, pp. 361–372, 17–21 February 1992, Ankara, Turkey.
Karabacak, V., Özkaymak, Ç., Sözbilir, H., Tatar, O., Aktuğ, B., Özdağ, Ö.C., Çakır, R., Aksoy, E., Koçbulut, F., Softa, M., Akgün, E., Demir, A., Arslan, G., 2023. The 2023

Pazarcık (Kahramanmaraş, Türkiye) earthquake (Mw: 7.7): implications for surface rupture dynamics along the East Anatolian Fault Zone. Geological Society of London Collection 180 (3), jgs2023, 020.
Karabulut, H., Bouchon, M., Schmittbuhl, J., 2022. Synchronization of small-scale seismic clusters reveals large-scale plate deformation. Earth Planets Space 74, 158. https://doi.org/10.1186/s40623-022-01725-z.
Karslıoğlu, A., Alkayış, M.H., Onur, M.i., 2021. Earthquake induced surface subsidence analysis with Sentinel-1 satellite: Sivrice-Doğanyol-Pütürge. Gümüşhane University Journal of Science and Technology 11 (2), 510–521.
Kaymakçı, N., İnceöz, M., Ertepinar, P., Koç, A., 2010. Late Cretaceous to Recent Kinematics of SE Anatolia (Turkey), vol. 340. Geological Society London, Special Issue, pp. 409–435.
Keller, E.A., 1986. Investigation of active tectonics: use of surficial earth processes. In: Wallace, R.E. (Ed.), Active Tectonics, Studies in Geophysics. National Academy Press, pp. 136–147.
Keller, E.A., Pinter, N., 1996. Active Tectonics: Earthquakes, Uplift, and Landscape. Prentice Hall, New Jersey.
Keller, E.A., Pinter, N., 2002. Active Tectonics: Earthquakes, Uplift, and Landscape, second ed. Prentice Hall, Upper Saddle River, America.
Ketin, İ., 1948. Son on yılda Türkiye'de vukua gelen büyük depremlerin tektonik ve mekanik neticeleri hakkında. Bull. Geol. Soc. Turk. 2 (1), 1–13.
Khalifa, A., Çakır, Z., Owen, L.A., Kaya, Ş., 2018. Morphotectonic analysis of the East Anatolian fault, Turkey. Turk. J. Earth Sci. 27 (2), 110–126.
Kiratzi, A., 1993. A study on the active crustal deformation of the North and East Anatolian fault zones. Tectonophysics 225, 191–203.
Kirby, E., Whipple, K., 2001. Quantifying differential rock-uplift rates via stream profile analysis. Geology 29 (5), 415–418.
Kirby, E., Whipple, K.X., 2012. Expression of active tectonics in erosional landscapes. J. Struct. Geol. 44, 54–75.
Koçyiğit, A., Yılmaz, A., Adamia, S., Kuloshvılı, S., 2001. Neotectonics of East Anatolian plateau (Turkey) and lesser caucasus: implication for transition from thrusting to strike-slip faulting. Geodin. Acta 14, 177–195.
Konca, A.Ö., Karabulut, H., Güvercin, S.E., Eskiköy, F., Özapacı, S., Özdemir, A., et al., 2021. From interseismic deformation with near-repeating earthquakes to co-seismic rupture: a unified view of the 2020 M_w6.8 Sivrice (Elazığ), Eastern Turkey Earthquake. J. Geophys. Res. Solid Earth 126, 10.
Koukouvelas, I.K., Zygouri, V., Nikolapoulos, K., Verroios, S., 2018. Treatise on the tectonic geomorphology of active faults: the significance of using a universal digital elevation model. J. Struct. Geol. 116, 241–252.
Kreemer, C., Blewitt, G., Klein, E.C., 2014. A geodetic plate motion and global strain rate model. G-cubed 15 (10), 3849–3889. https://doi.org/10.1002/2014GC005407.
Kürçer, A., Elmacı, H., Yıldırım, N., Özalp, S., Domaç-Yalçın, H., 2020. 24 ocak 2020 Sivrice (Elazığ) depremi (Mw: 6.8-6.5) saha gözlemleri ve değerlendirme, doğu anadolu fay zonu, Türkiye. ATAG (Aktif Tektonik Araştırma Grubu) 2020, Özel Toplantısı Bildiri Özleri.
Kurt, A.İ., Özbakır, A.D., Cingöz, A., Ergintav, S., Doğan, U., Özarpacı, S., 2023. Contemporary velocity field for Turkey inferred from combination of a dense network of long term GNSS observations. Turk. J. Earth Sci. 32 (3), 4.
Li, X., Zhang, H., Su, Q., 2019. Bedrock channel form in the madong Shan (NE tibet): implications for the strain transfer along the strike-slip Haiyuan Fault. J. Asian Earth Sci. 181.
Londono, S.N., Restrepo-Moreno, S.A., Vinasco, C., Bermudez, M.A., Min, K., 2020. Thermochronologic and geomorphometric constraints on the cenozoic landscape evolution of the northern andes: northwestern central cordillera, Colombia. Geomorphplogy 351, 106890.
Lovelock, P.E.R., 1984. A review of the tectonics of the northern Middle East region. Geol. Mag. 121 (6), 577–587.
Lyberis, N., Yürür, T., Chorowicz, J., Kasapoğlu, E., Gündoğdu, N., 1992. The East Anatolian Fault: an oblique collisional belt. Tectonophysics 204, 1–15.
Magen, Y., Baer, G., Ziv, A., Inbal, A., Nof, R.N., Hamiel, Y., Piatibratova, O., Gürbüz, G., 2024. Fault coalescence, slip distribution, and stress drop of the february 2023 southeast Türkiye earthquakes from joint inversion of SAR, GNSS, and burst overlap interferometry. Seismol Res. Lett. 95 (2A), 680–696. https://doi.org/10.1785/0220230271.
Mayer, L., 1986. Tectonic geomorphology of escarpments and mountain fronts. In: Wallace, R.E. (Ed.), Active Tectonics, Studies in Geophysics, 1 st ed. National Academy Press, Washington, D.C, p. 125. 135.
McClusky, S., Balassanian, S., Barka, A.A., Demir, C., Ergintav, S., Georgiev, I., Gürkan, O., Hamburger, M., Hurst, K., Kahle, H., Kastens, K., Kekelidze, G., King, R. W., Kotzev, V., Lenk, O., Mahmoud, S., Mıshın, A., Nadaria, M., Ouzounıs, A., Paradıssıs, D., Peter, Y., Prelepin, M., Reilinger, R.E., Şanlı, I., Seeger, H., Tealeb, A., Toksöz, M.N., Veis, G., 2000. Global positioning system consraints on plate kinematics and dynamics in the eastern Mediterranean and Caucasus. J. Geophys. Res. C Oceans Atmos. 105, 5685–5719.
McKenzie, D.P., 1970. Plate tectonics of the Mediterranean region. Nature 220, 239–343.
McKenzie, D.P., 1972. Active tectonics of the Mediterranean region. Geophys. J. Roy. Astron. Soc. 30, 109–185.
McKenzie, D.P., 1978. Some remarks on the development of sedimentary basins. Earth Planet Sci. Lett. 40, 25–32. https://doi.org/10.1016/0012-821X(78)90071-7.
Menéndez, M., Méndez, F.J., Losada, I.J., Graham, N.E., 2008. Variability of extreme wave heights in the northeast Pacific Ocean based on buoy measurements. Geophys. Res. Lett. 35, L22607.
Muehlberger, W.R., Gordon, M.B., 1987. Observation on the complexity of the East Anatolian fault, Turkey. J. Struct. Geol. 9 (7), 899–903.
Navabpour, P., Angelier, J., Barrier, E., 2007. Cenozoic post-collisional brittle tectonic history and stress reorientation in the High Zagros Belt (Iran, Fars Province). Tectonophysics 432 (1–4), 101–131.
Oral, M.B., Reilinger, R., Toksöz, R., 1992. Deformation of the Anatolian block as deduced from GPS measurements, Transactions. American Geophysical Union 73, 120. EOS.
Ouimet, W.B., Whipple, K.X., Granger, D.E., 2009. Beyond threshold hillslopes: channel adjustment to base-level fall in tectonically activemountain ranges. Geology 37 (7), 579–582. https://doi.org/10.1130/G30013A.1.
Özarpacı, S., Hofstetter, C., Funning, G., Dogan, U., Ergintav, S., Çakır, Z., Zabcı, C., Özdemir, A., Ayruk, E.T., Farımaz, İ., 2024. Creeping Pütürge segment with geodetic evidence. EGU General Assembly 2024, EGU24–19720. https://doi.org/10.5194/egusphere-egu24-19720. Vienna, Austria, 14–19 Apr 2024, 2024.
Özener, H., Arpat, E., Ergintav, S., Doğru, A., Çakmak, R., Turgut, B., Doğan, U., 2010. Kinematics of the eastern part of the North anatolian Fault Zone. J. Geodyn. 49 (3–4), 141–150.
Perinçek, D., Çemen, İ., 1990. The structural relationship between the East Anatolian and Dead Sea Fault zones in southeastern Turkey. Tectonophysics 172, 331–340.
Perron, J.T., Royden, L., 2013. An integral approach to bedrock river profile analysis. Earth Surf. Process. Landforms 38 (6), 570–576.
Pike, R.J., Wilson, S., 1971. Elevation-Relief ratio, hypsometric integral, and geomorphic area-altitude analysis. GSA Bulletin 82 (4), 1079–1084.
Pousse-Beltran, L., Nissen, E., Bergman, E.A., Cambaz, M.D., Gaudreau, É., Karasözen, E., Tan, F., 2020. The 2020 Mw 6.8 Elazığ (Turkey) earthquake reveals rupture behavior of the East Anatolian Fault. Geophys. Res. Lett. 47. https://doi.org/10.1029/2020GL088136.
Reilinger, R., McClusky, S., Vernant, P., Lawrence, S., Ergintav, S., Cakmak, R., Ozener, H., Kadirov, F., Guliev, I., Stepanyan, R., Nadariya, M., Hahubia, G., Mahmoud, S., Sakr, K., ArRajehi, A., Paradissis, D., Al-Aydrus, A., Prilepin, M., Guseva, T., Evren, E., Dmitrotsa, A., Filikov, S.V., Gomez, F., Al-Ghazzi, R., Karam, G., 2006. GPS constraints on continental deformation in the Africa-Arabia-Eurasia continental collision zone and implications for the dynamics of plate interactions. J. Geophys. Res. Solid Earth 111 (B5). Art. B05411, 52.
Ren, C., Wamg, Z., Taymaz, T., Hu, N., Luo, H., Zhao, Z., Yue, H., Song, X., Shen, Z., Xu, H., Geng, J., Zhang, W., Wang, T., Ge, Z., Irmak, T.S., Erman, C., Zhou, Y., Li, Z., Xu, H., Cao, B., Ding, H., 2023. Supershear triggering and cascading fault ruptures of the 2023 Kahramanmaraş, Türkiye, Earthquake doublet. Nat. Hazards 383, 305–311.
Rockwell, T.K., Keller, E.A., Clark, M.N., Johnson, D.L., 1984. Chronology and rates of faulting of Ventura River terraces, California. Geol. Soc. Am. Bull. 95 (12), 1466–1474.
Roe, G.H., Montgomery, D.R., Hallet, B., 2003. Orographic precipitation and the relief of mountain ranges. J. Geophys. Res. 108 (B6), 2315.
Şaroğlu, F., Emre, Ö., Kuşçu, İ., 1992. The East Anatolian fault zones of Turkey. Ann. Tect. 6, 99–125.
Schwanghart, W., Kuhn, N.J., 2010. TopoToolbox: a set of MATLAB functions for topographic analysis. Environ. Model. Software. https://doi.org/10.1016/j.envsoft.2009.12.002.
Schwanghart, W., Scherler, D., 2014. TopoToolbox 2–MATLAB-based software for topographic analysis and modelling in Earth surface sciences. Earth Surf. Dyn. 2 (1), 1–7. https://doi.org/10.5194/esurf-2-1-2014.
Scotti, V.N., Molin, P., Faccenna, C., Soligo, M., Casas-Sainz, A., 2014. The influence of surface and tectonic processes on landscape evolution of the Iberian Chain (Spain): quantitative geomorphological analysis and geochronology. Geomorphology 2014, 37–57.
Selby, M.J., 1980. A rock strength classifcation for geomorphic purposes: with tests from Antarctica and New Zealand. Geomorphology 24, 31–51.
Şengör, A.M.C., 1980. Principles of the neotectonism of Turkey. Türkiye Jeoloji Kurumu Konferans Serisi 2. Ankara, Turkey.
Şengör, A.M.C., Yılmaz, Y., 1981. Tethyan evolution of Turkey; a plate tectonic approach. Tectonophysics 75 (3–4), 181–241.
Şengör, A.M.C., Görür, N., Şaroğlu, F., 1985. Strike-slip faulting and related basin formation in zones of tectonic escape: Turkey as a case study. In: Biddle, K.T. (Ed.), Strike-slip Deformation, Basin Formation, and Sedimentation, Soc. Econ. Paleontol. Spec. Publ. Editör. Christie-Blick, N. Oklahoma: Society of Economic Paleontologists and Mineralogists, Special Publication, pp. 227–264.
Seymen, İ., Aydın, A., 1972. Bingöl deprem fayi ve bunun Kuzey Anadolu fay zonu ile ilişkisi. Bulletin of the Mineral Research and Exploration 79 (79), 1–12.
Softa, M., 2022. Morphometric and kinematic analysis of southern margin of the Küçük Menderes Graben and its tectonic implications in western Anatolia. Arabian J. Geosci. 15, 131.
Softa, M., Emre, T., Sözbilir, H., Spencer, J.Q.G., Turan, M., 2018. Geomorphic evidence for active tectonic deformation in the coastal part of Eastern Black Sea, Eastern Pontides, Turkey. Geodin. Acta 30 (1), 249–264.
Softa, M., Kocbulut, F., Akgün, E., Aksoy, E., Sözbilir, H., Tatar, O., Karabacak, V., Özkaymak, Ç., Utku, M., Özdağ, Ö.C., Çakır, R., Demir, A., Arslan, G., 2024. Surface rupture during the 6th of February 2023 Mw 7.6 Elbistan-Ekinözü. (Kahramanmaraş) earthquake: implications for fault rupture dynamics along the northern branch of East Anatolian Fault Zone. Turk. J. Earth Sci. 33 (1), 1–21.
Sun, L., Mann, P., 2021. Along-strike rapid structural and geomorphic transition from transpression to strike-slip to transtension related to active microplate rotation, Papua New Guinea. Front. Earth Sci. 9, 652352. https://doi.org/10.3389/feart.2021.652352.
Tan, O., Tapirdamaz, M.C., Yörük, A., 2008. The earthquake catalogs for Turkey. Turk. J. Earth Sci. 17, 405–418.
Tatar, O., Sözbilir, H., Koçbulut, F., Bozkurt, E., Aksoy, E., et al., 2020. Surface deformations of 24 january 2020 Sivrice (Elazığ)- doğanyol (Malatya) earthquake

(Mw=6.8) along the Pütürge segment of the East Anatolian Fault Zone and its comparison with Turkey's 100- year-surface rupture. Mediterranean Geoscience Reviews 2 (3), 385–410.
Taymaz, T., Eyidoğan, H., Jackson, J., 1991. Source parameters of large earthquakes in the East Anatolian Fault Zone (Turkey). Geophys. J. Int. 106, 537–550.
Topal, S., Softa, M., 2023. Geomorphic signature of active tectonics in Simav Graben: an evaluation of indicator relative tectonic activity of Simav Fault and its seismotectonic implications for Western Anatolia. J. Earth Syst. Sci. 132, 95, 2023.
Topal, S., Keller, E., Bufe, A., Koçyiğit, A., 2016. Tectonic geomorphology of a large normal fault: akşehir fault, SW Turkey. Geomorphology 259, 55–69.
USGS, 2023. United States Geological Survey [Online]. Website. http://earthquake.usgs.gov. (Accessed 13 February 2023).
Vanik, N., Shaikh, H., Mukherjee, S., Maurya, D.M., Chamyal, L.S., 2018. Post-Deccan trap stress reorientation under transpression: evidence from fault slip analyses from SW Saurashtra, western India. J. Geodyn. 121, 9–19.
Wallace, R.E., 1958. Geometry of shearing stress and relation to faulting. J. Geol. 59, 118.
Walters, R.J.B., Parsons, Wright, T.J., 2014. Constraining crustal velocity fields with InSAR for Eastern Turkey: limits to the block-like behavior of Eastern Anatolia. J. Geophys. Res. 119, 5215–5234.
Wang, J., Hu, Z., Pan, B., Li, M., Dong, Z., Li, X., Li, X., Bridgland, D., 2019. Spatial distribution pattern of channel steepness index as evidence for differential rock uplift along the eastern Altun Shan on the northern Tibetan Plateau. Global Planet. Change 181.
Westaway, R., 1994. Present-day kinematics of the Middle East and eastern mediterranean. Journal Geophysics Research 99, 2071–2090.
Westaway, R., 2003. Kinematics of the Middle East and eastern mediterranean updated. Turkish J.Earth Sci. J. 12, 5–46.
Westaway, R., 2004. Kinematic consistency between the Dead Sea Fault zone and the neogene and quaternary left-lateral faulting in SE Turkey. Tectonophysics 391, 203–237.
Westaway, R., 2006. Late Cenozoic extension in southwest Bulgaria: a synthesis. In: Robertson, A.H.F., Mountrakis, D. (Eds.), Tectonic Development of the Eastern Mediterranean Region, vol. 260. Geological Society, London, Special Publications, pp. 557–590.
Westaway, R., Arger, J., 1996. The Gölbaşı basin, southeastern Turkey: a complex discontinuity in a major strike-slip fault zone. J. Geol. Soc. (Lond.) 153, 729–743.
Westaway, R., Arger, J., 2001. Kinematics of the malatya–ovacik fault zone. Geodin. Acta 14 (1–3), 103–131.
Whipple, K.X., 2009. The influence of climate on the tectonic evolution of mountain belts. Nat. Geosci. 2, 97–104.
Whipple, K.X., Tucker, G.E., 1999. Dynamics of the stream-power river incision model: implications for height limits of mountain ranges, landscape response timescales, and research needs. J. Geophys. Res. Solid Earth 104, 17661–17674. https://doi.org/10.1029/1999JB900120.
Whipple, K.X., DiBiase, R.A., Crosby, B., 2013. In: Shroder, J.J., Wohl, E. (Eds.), Bedrock Rivers, inTreatise on Fluvial Geomorphology, vol. 9. Academic Press, San Diego, Calif, pp. 550–573. https://doi.org/10.1016/B978-0-12-374739-6.00254-2.
Whipple, K.X., Forte, A.M., DiBiase, R.A., Gasparini, N.M., Ouimet, W.B., 2017. Timescales of landscape response to divide migration and drainage capture: implications for the role of divide mobility in landscape evolution. J. Geophys. Res.: Earth Surf. 122 (1), 248–273. https://doi.org/10.1002/2016JF003973.
Whittaker, A.C., Cowie, P.A., Attal, M., Tucker, G.E., Roberts, G.P., 2008. Bedrock channel adjustment to tectonic forcing: implications forpredicting river incision rates. Geology 35 (2), 103–106. https://doi.org/10.1130/g20738.1.
Willett, S.D., 1999. Orogeny and orography: the effects of erosion on the structure of mountain belts. J. Geophys. Res. 104, 28957–28981. https://doi.org/10.1029/1999JB900248.
Willett, S.D., Hovius, N., Brandon, M., Fisher, D.M., 2006. Tectonics, Climate, and Landscape Evolution, vol. 398. Geological Society of America Special Paper.
Willett, S.D., Mccoy, S.W., Perron, J.T., Goren, L., Chen, C.Y., 2014. Dynamic reorganization of river basins. Science 343, 1248765. https://doi.org/10.1126/science.1248765.
Wobus, C.W., Tucker, G.E., Anderson, R.S., 2006. Self-formed bedrock channels. Geophys. Res. Lett. 33.
Yazıcı, M., Zabcı, C., Sançar, T., Natalin, B.A., 2018. The role of intraplate strike-slip faults in shaping the surrounding morphology: the Ovacık Fault (eastern Turkey) as a case study. Geomorphology 321, 129–145.
Yılmaz, Y., 1993. New evidence and model on the evolution of the southeast Anatolian orogen. Geol. Soc. Am. Bull. 105, 251–271.
Yönlü, Ö., Karabacak, V., Altunel, E., Akyüz, H.S., 2012. Paleoseismological slip rate on the East Anatolian Fault Zone around Türkoğlu. International Earth Science Colloquium on the Aegean Region. IESCA-2012, 1–5 October 2012, İzmir.
Yürür, M.T., Chorowicz, J., 1998. Recent volcanis, tectonics and plate kinematics near the junction of the African, Arabian Anatolian plates in the eastern Mediterranean. Jour. Volcanol. Geotherm. Rec. 85, 1–15.
Zabcı, C., 2020. Malatya Fayı'nın morfometrik özellikleri. Türk Coğrafya Dergisi 75, 107–118.